Asian Journal of Chemistry; Vol. 38, No. 11 (2026), 2854-2876
ASIAN JOURNAL OF CHEMISTRY
https://doi.org/10.14233/ajchem.2026.36879

REVIEW

Synthesis Strategies and Photocatalytic Efficiency of Bi_2O_3 based Nanostructures: A Comprehensive Review on Recent Progress and Applications in Dye Degradation, CO_2 Reduction and Hydrogen Generation

ANKITA MEHER and DOJALISA SAHU*

School of Applied Sciences, Centurion University of Technology and Management P.O. Jatni, Bhubaneswar-752050, India

*Corresponding author: E-mail: dojalisa.sahu@cutm.ac.in

Received: 23 July 2026 *Accepted*: 30 October 2026 *Published online*: 13 November 2026 AJC-22516

Bismuth oxide (Bi_2O_3) based nanomaterials have emerged as promising visible light driven photocatalysts for different applications like wastewater treatment, CO_2 reduction and hydrogen generation. This is possible due to their suitable band structure, strong visible light absorption and chemical stability. This review presents a critical assessment of recent advances in the synthesis, modification and photocatalytic applications of Bi_2O_3 nanostructures for the degradation of organic dyes, pharmaceutical residues and other emerging pollutants. Major synthesis routes, such as sol-gel, hydrothermal, solvothermal, chemical precipitation and green synthesis, are discussed in relation to their effects on crystal structure, morphology, surface properties and photocatalytic performance. Strategies to address the inherent limitations of pristine Bi_2O_3 are examined, with particular emphasis on elemental doping and heterojunction engineering. Recent developments in Bi_2O_3-based composites incorporating semiconductors such as TiO_2, *g*-C_3N_4 and MoS_2 are reviewed, with attention to interfacial charge transfer and improved charge-carrier separation. The fundamental aspects of photocatalysis, such as charge-carrier dynamics, reactive oxygen species formation and interfacial electron-transfer processes, are critically discussed. The scope of the review extends beyond pollutant degradation to the application of Bi_2O_3-based nanostructures in photocatalytic CO_2 reduction and water splitting, with particular focus on solar-driven hydrogen generation, material modification and surface reaction pathways. The existing limitations in photocatalytic efficiency, structural stability and practical applicability are assessed, along with future research directions for the design of efficient, durable and scalable Bi_2O_3-based photocatalysts for environmental remediation and solar energy conversion.

Keywords: Bismuth oxide, Photocatalysis, Heterojunction nanocomposites, Doping, Environmental remediation.

INTRODUCTION

Over the last few years, researchers have exhibited a strong interest in bismuth based compounds that respond to visible light. These comprise substances such as bismuth tungstate, bismuth oxide, bismuth vanadate and bismuth molybdate [1]. Amongst these materials, bismuth oxide nanoparticles (Bi_2O_3 NPs) are attracting significant attention among numerous Bi based materials with a rising order of publications from 2000 to 2025 (Fig. 1). It shows a year by year breakdown of publications on bismuth based articles, which was collected from the major database, web of science, Scopus, google scholar, *etc*. Due to its distinct pair of $6s^2$ electrons in bismuth oxide that acts as a *p*-type semiconductor, strongly repelling nearby chemical bonds. Presently garnering interest as a promising photocatalyst for several real-world applications (solar cells, gas detection sensors, fuel cell technology, supercapacitors and photocatalytic applications) owing to a direct band gap of around 2.8 eV [2-4].

Over the past few decades, the environmental impacts of extensive antibiotic and dye use in around 80% of enterprises have become a major problem, posing risks to human health. Various treatment techniques have been used to reduce water pollution, thereby decreasing human illnesses and environmental damage [5]. Filtration, adsorption, disinfection and advanced oxidation processes (AOPs) have all been found to be viable wastewater treatment approaches [6,7]. In order to break down organic contaminants, microorganisms and disinfectant byproducts, AOPs primarily depend on the *in situ* production of extremely reactive species [8]. Photocatalysis is an

This is an open access journal, and articles are distributed under the terms of the Attribution 4.0 International (CC BY 4.0) License. This license lets others distribute, remix, tweak, and build upon your work, even commercially, as long as they credit the author for the original creation. You must give appropriate credit, provide a link to the license, and indicate if changes were made.

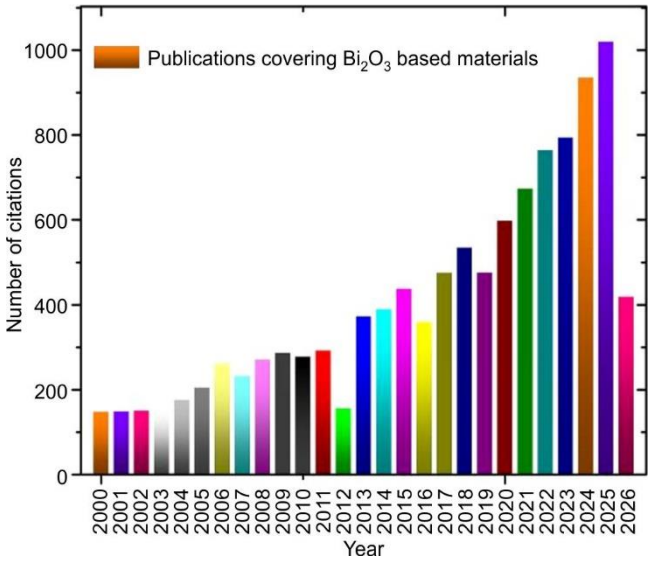


Fig. 1. Year wise literature studied and reviewed on Bi_2O_3 based papers

AOP in which a semiconductor photocatalyst absorbs photons with sufficient energy to excite electrons from the valence band (VB) to the conduction band (CB). Further, electron (e^-)-hole (h^+) pairs are developed that drive subsequent redox reactions [2,3]. Specifically, a range of organic pollutants involves decomposing or being converted into byproducts such as CO_2 and H_2O during the AOPs and photocatalytic methods. Among the many photocatalyst semiconductor based photocatalysts are attracting a lot of interest due to their superior photocatalytic activity [9].

Pristine Bi_2O_3 exhibits lower than expected photocatalytic activity, mainly due to the rapid recombination of photo-induced electrons and holes. Its conduction band potential (0.33 V) is insufficient for oxygen reduction through the single electron pathway (-0.56 V) and presents limitations for the four-electron reduction pathway (+0.40 V) [10-15]. Several methods have been investigated to overcome these limitations such as microstructure regulation, noble metal deposition, metal and non-metal doping and the formation of composites and heterostructures with other compounds [2-4]. The synthesis method plays an important role in determining the morphology, crystal structure and surface characteristics of Bi_2O_3. Recent studies have shifted towards the development of complex photocatalytic systems beyond conventional binary combinations, with an emphasis on improved structural stability, broader spectral absorption and efficient charge transfer. Heterojunctions with complementary absorption ranges offer opportunities for better utilization of the solar spectrum, particularly in photocatalytic hydrogen peroxide production [16-18]. Defect engineering through the introduction of oxygen vacancies and multiple dopant elements has been investigated as a means of improving charge separation and photocatalytic activity [3].

The incorporation of metal oxides, carbon-based substrates and other functional support materials into Bi_2O_3 composites has improved pollutant removal, adsorption capacity and charge transport under practical treatment conditions. Several reported systems retain their photocatalytic performance over repeated cycles, making them promising candidates for wastewater treatment [2,3,19,20]. The applications of Bi_2O_3-based materials extend beyond environmental remediation to sensing, energy storage, biomedical applications, optoelectronics and electronic devices, as schematically illustrated in Fig. 2. Elemental doping, morphology engineering and heterostructure formation with suitable semiconductors or carbon-based materials are widely investigated approaches for modifying the photocatalytic properties of Bi_2O_3. Elemental doping alters the electronic structure, introduces defect states and can improve visible-light absorption. Heterostructure engineering facilitates interfacial charge transfer, promotes charge carrier separation and reduce electron-hole recombination [2-4,21,22]. The combined use of these modification strategies provides scope for improving photocatalytic efficiency, visible light responsiveness, structural stability and the degradation of organic pollutants and emerging water contaminants [21,22].

Research on Bi_2O_3-based photocatalysts has largely examined individual aspects, such as crystal structure, synthesis methods, elemental doping and heterojunction engineering, with limited attention to the relationships between these factors and photocatalytic performance. Systematic comparisons of pristine, doped and heterostructured Bi_2O_3 are still relatively scarce. The present review addresses this gap through a critical assessment of the literature published up to 2026. It covers crystal structures, synthesis strategies, material modification approaches, photocatalytic mechanisms and recent developments in Bi_2O_3-based nanostructures. Particular attention is given to the relationship between structural and electronic modifications and photocatalytic performance, along with the major challenges and future research directions for practical wastewater treatment applications.

Method: This study systematically reviews recent research on Bi_2O_3-based nanostructures and nanocomposites for photocatalytic environmental remediation. Rayyan software (version 2026) was used for collaborative screening and study selection according to predefined inclusion and exclusion criteria [23]. The blind mode was enabled to minimize selection bias through independent assessment. Titles and abstracts were screened initially, followed by full-text eligibility assessment and data extraction. Information on Bi_2O_3 nanoparticles, synthesis methods, nanocomposite development and environmental applications was compiled in Microsoft Excel for comparative analysis. The initial Scopus search identified 641 records (database, n = 641; registries, n = 558). Before screening, 94 records related to multiple keywords and 69 publications outside the 2020-2026 period were excluded, leaving 395 records. Ten previously identified relevant articles were added, bringing the total to 405 records. Of these, 35 were excluded based on publication type and 19 through automated screening, leaving 351 reports for retrieval. Following the exclusion of 27 reports due to unavailable full texts, 324 reports underwent eligibility assessment. Of these, 71 were excluded for being outside the materials science scope (n = 71) or not directly related to Bi_2O_3/Bi_2O_3-based nanocomposites (n = 36). Consequently, 217 studies were considered relevant to the systematic review, of which 164 met the inclusion criteria and were selected for final analysis. The complete study selection process and reasons for exclusion are presented in the PRISMA flow diagram (Fig. 3).



Fig. 2. Schematic diagram showing various applications of Bi_2O_3 nanostructures

Crystal structure and structural properties of Bi_2O_3: Bi_2O_3 is a polymorphic semiconductor that has attracted considerable research interest due to its diverse crystal structures, tunable electronic properties and good physico-chemical stability [2-4,24,25]. Its relatively narrow band gap (2.1-2.8 eV), high refractive index and large dielectric constant make it a promising material for optical, electronic, sensing and energy related applications [3,4]. Its electronic characteristics are strongly influenced by the stereochemically active Bi $6s^2$ lone pair electrons and their interaction with O 2*p* orbitals. This orbital hybridization contributes to lattice distortion and modifies the electronic band structure, which influence the optical and electrical properties of Bi_2O_3 [26-30].

The structural and electronic properties of Bi_2O_3 are closely related to its crystallographic phase. It exists in six polymorphs: monoclinic (α), tetragonal (β), body-centred cubic (γ), face-centred cubic (δ), orthorhombic (ε) and triclinic (ω) [2-4,10]. Among these, the α-, β-, γ- and δ-phases have been investigated most extensively due to their distinct structural and electronic characteristics. The monoclinic α-phase is thermodynamically stable at room temperature, whereas the β-, γ- and δ-phases are generally metastable at lower temperatures or stable at elevated temperatures. Suitable synthesis conditions and quenching processes can help retain these metastable phases [2-4]. The crystal structures of α-Bi_2O_3, β-Bi_2O_3, γ-Bi_2O_3 and δ-Bi_2O_3 are shown in Fig. 4a-d, respectively [31].

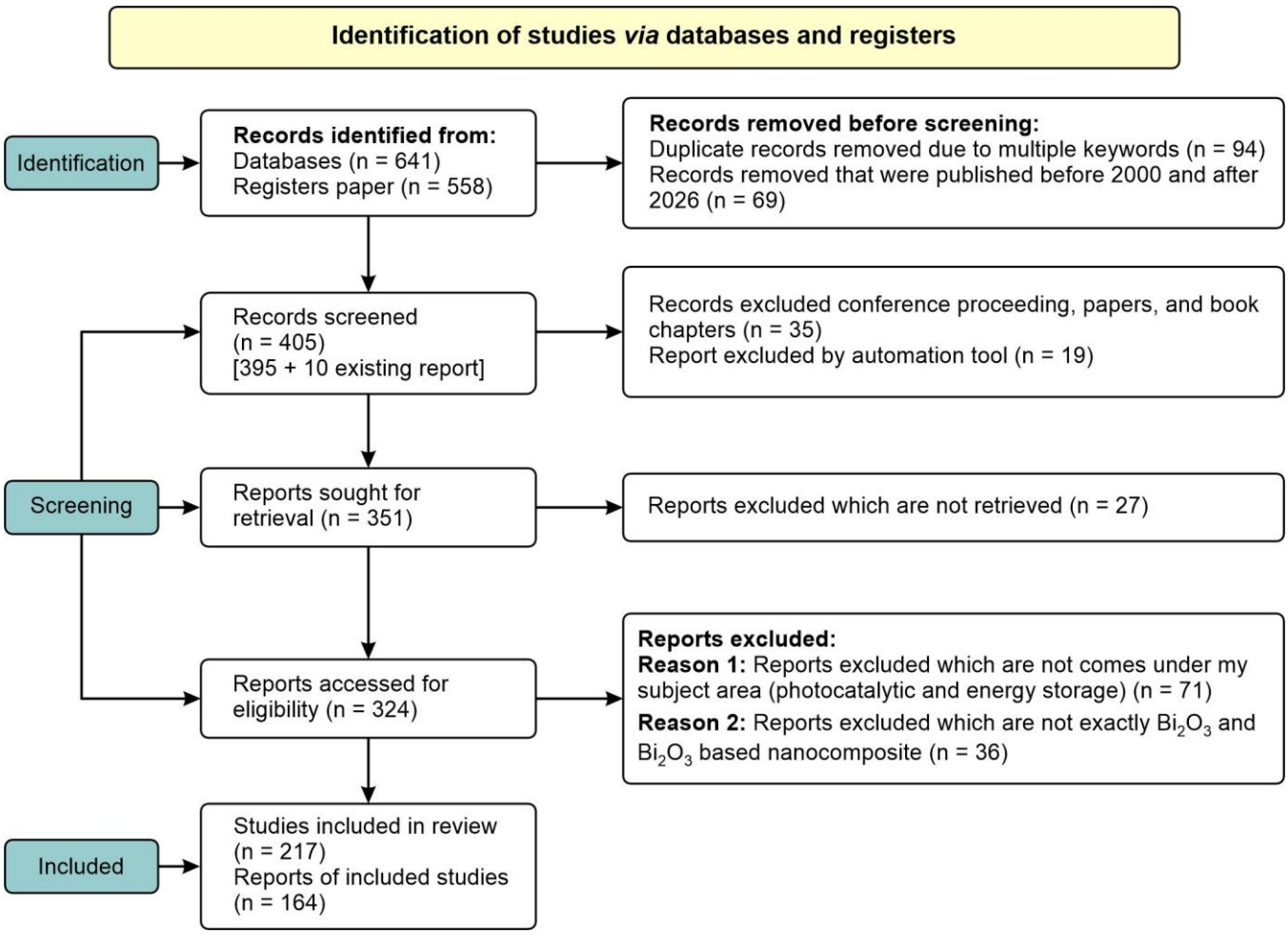


Fig. 3. PRISMA flow chart diagram for selecting articles for the review

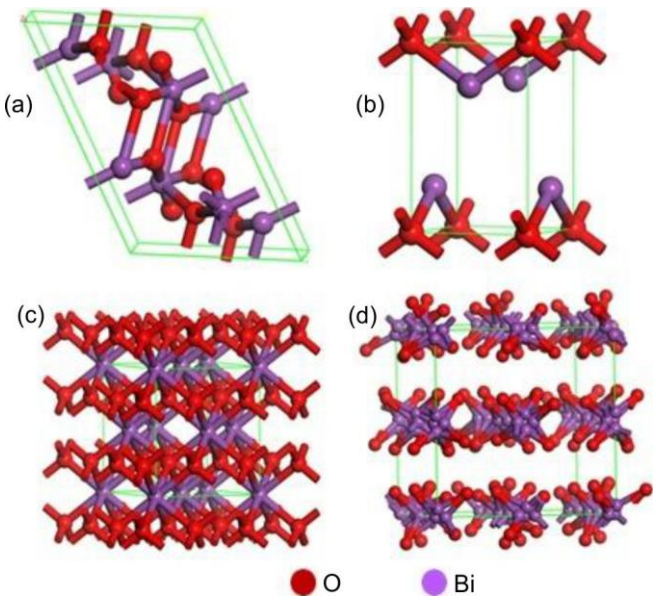


Fig. 4. Schematics of the crystal structures α-Bi_2O_3 (a), β-Bi_2O_3 (b), γ-Bi_2O_3 (c) and δ-Bi_2O_3 (d)

The differences in crystal symmetry, phase composition and intrinsic lattice defects, particularly oxygen vacancies, influence the electronic structure, structural stability and charge carrier behaviour of individual Bi_2O_3 polymorphs [26-30]. The valence band maximum has been reported at approximately +3.13 V *versus* the normal hydrogen electrode (NHE), while the conduction band position varies with the crystallographic phase [32-38]. These variations are important in determining light absorption, charge separation and the feasibility of surface redox reactions. The phase-dependent electronic structure, together with the influence of lattice defects and orbital interactions, provides the basis for tailoring Bi_2O_3 through controlled synthesis, elemental doping and heterostructure engineering for improved photocatalytic applications.

Synthesis strategies for Bi_2O_3-based nanostructures: The synthesis approach plays a decisive role in defining the physico-chemical characteristics of Bi_2O_3 by regulating its crystal structure, morphology, particle dimensions, surface characteristics, defect population and interfacial properties [3,4,10,39]. Since these structural features directly determine light absorption, charge carrier dynamics and surface reaction kinetics, the selection of an appropriate synthesis method has become a critical aspect in designing effective Bi_2O_3 based photocatalysts [3,4,22,39]. Over the past two decades, numerous physical, chemical and green synthetic methods have been developed to fabricate pure Bi_2O_3, doped Bi_2O_3 and Bi_2O_3 based heterostructures with tailored structural and electronic properties [2-4]. The versatility of these synthesis strategies

has enabled the preparation of Bi_2O_3 in diverse architectures including nanoparticles, nanorods, nanowires, nanotubes, nanoflowers, nanosheets, hollow spheres, thin films, porous frameworks and hierarchical three-dimensional assemblies, each offering unique advantages. The synthesis of pure Bi_2O_3 is primarily directed toward controlling its crystal phase, morphology and crystallinity, whereas doped Bi_2O_3 and Bi_2O_3 based heterostructures are designed to tailor the electronic structure, facilitate charge separation and extend visible-light absorption. Consequently, strategies such as elemental doping and coupling Bi_2O_3 with semiconductors, carbon materials, metal oxides, sulphides or MOFs have become effective methods for enhancing photocatalytic performance through the formation of p-n, type-II, Schottky, Z-scheme and S-scheme heterojunctions [2-4,7].

The synthesis of Bi_2O_3 nanostructures involves a range of chemical and physical approaches, each offering different possibilities for controlling particle morphology, crystallinity, composition and surface properties. Wet chemical routes are particularly popular due to their relatively simple procedures, low processing costs and adaptability to large-scale production [10,40,41]. Their ability to regulate nucleation and crystal growth makes them suitable for preparing nanoparticles with controlled dimensions, doped compositions and multicomponent heterostructures. The sol-gel process is widely employed for this purpose, as molecular-level mixing of precursor materials promotes compositional uniformity and precise stoichiometric control [2,3]. Other synthesis routes such as chemical precipitation, co-precipitation, microemulsion, microwave-assisted synthesis, sonochemical processing, combustion and template-assisted methods, offer additional control over particle formation and morphology [2-4,10].

A different approach is adopted when Bi_2O_3 is required in the form of thin films or surface coatings. Techniques such as pulsed laser deposition, sputtering, CVD, thermal evaporation, PVD and electrodeposition are commonly used to fabricate such structures for photoelectrochemical, sensing and optoelectronic applications [2-4,10]. Their ability to regulate film thickness, surface uniformity and crystallinity is particularly useful in device fabrication. The requirement for specialized equipment, controlled processing environments and higher fabrication costs can restrict their use in the production of bulk photocatalyst powders. The following sections examine these synthesis routes in terms of their underlying principles, material formation processes, advantages and limitations, with particular reference to their suitability for pristine, doped and heterostructured Bi_2O_3 photocatalysts.

Sol-gel method: The sol-gel method is a simple technique for preparing nanomaterials with excellent compositional control and high homogeneity [42]. In this approach, metal precursors are initially dissolved to form a stable sol, which subsequently undergoes hydrolysis and polycondensation reactions to generate a three-dimensional gel network [43,44].

The resulting gel is then subjected to drying and calcination, where the organic constituents are removed and crystalline material is formed. The method provides precise control over stoichiometry and enables the synthesis of nanostructures with tunable morphology, making it particularly suitable for preparing pure, doped and composite Bi_2O_3 materials [43-49]. Khairnar & Shrivastava [44] studied the photocatalytic decomposition of methylene blue and chlorpyrifos by α-Bi_2O_3 that was synthesized by sol-gel method [44]. Most recently, a facile sol-gel synthesis reported by Aksit *et al.* [48] yielded tetragonal Bi_2O_3 nanostructures possessing flower- and needle-like morphologies. These uniquely structured photocatalysts exhibited exceptional activity under sunlight, leading to the rapid and complete degradation of paracetamol within 15 min [48].

Co-precipitation method: Uniform nucleation and precise compositional control are important considerations in the synthesis of Bi_2O_3 photocatalysts with tailored structural and morphological properties [50-54]. Co-precipitation is a widely employed wet-chemical approach, as the simultaneous precipitation of metal ions promotes homogeneous precursor formation and controlled crystal growth. The synthesis generally involves dissolving suitable metal salts in an aqueous medium followed by the gradual addition of a precipitating agent to initiate nucleation [55]. The resulting precipitate undergoes aging, filtration or centrifugation, repeated washing, drying and subsequent calcination to obtain crystalline Bi_2O_3. The final phase, particle size and morphology are strongly influenced by precursor concentration, solution pH, precipitation rate, aging duration and calcination temperature. Its relatively mild reaction conditions and limited equipment requirements make co-precipitation a convenient route for preparing Bi_2O_3 nanostructures [55]. The method is particularly suitable for introducing foreign metal ions into the oxide lattice and preparing multicomponent oxide systems with modified optical and electronic properties [54].

Several studies have explored the influence of synthesis conditions and precursor additives on the structural characteristics of Bi_2O_3. Essenni *et al.* [50] synthesized α-Bi_2O_3 nanoparticles through a precipitation-assisted method using chitosan and sodium alginate as biodegradable templating agents to regulate crystal growth and morphological development. In another study, Divya *et al.* [51] prepared needle-shaped α-Bi_2O_3 nanoparticles through co-precipitation followed by annealing at temperatures ranging from 200 to 700 ºC. The annealing treatment resulted in a reduction in the band gap from 2.90 to 2.81 eV.

Solvothermal and hydrothermal methods: The solvothermal and hydrothermal methods are among the most effective solution based techniques for synthesizing Bi_2O_3 NPs, since they offer good control over crystal structure, morphology, particle size and purity [56-64]. Both methods rely on chemical reactions occurring in a sealed autoclave at temperatures above the boiling point of the solvent, where the resulting autogenous pressure accelerates nucleation and crystal growth. Compared with conventional synthesis routes, these methods yield highly crystalline nanomaterials under relatively mild conditions while minimizing contamination. The major difference between the two approaches is the reaction medium [56,57].

In hydrothermal synthesis, water serves as the reaction solvent, whereas solvothermal synthesis is performed using organic solvents such as ethanol, methanol, ethylene glycol, or glycerol. Solvent selection plays an important role in solvothermal synthesis, as it determines the reaction environment and influences precursor solubility, nucleation, crystal growth and the physico-chemical characteristics of the resulting Bi_2O_3.

The process generally involves dissolving a bismuth precursor, commonly bismuth nitrate, in a suitable solvent, followed by treatment under controlled temperature and pressure. During the reaction, hydrolysis and condensation of Bi^{3+} species lead to the formation of nuclei, which subsequently develop into crystalline particles. The resulting morphology is governed by the interplay between nucleation and crystal growth, with precursor concentration, solvent composition, reaction temperature, pressure and treatment duration serving as important controlling parameters. Appropriate adjustment of these conditions allows the formation of different Bi_2O_3 architectures such as nanoparticles, nanosheets, nanoflowers, nanorods and hierarchical structures. The synthesized material is generally subjected to washing, drying and where necessary, calcination to improve crystallinity and obtain the desired crystalline phase [56-64].

The versatility of this approach has been explored in the preparation of Bi_2O_3-based composite materials. Li *et al*. [57] employed a two-step solvothermal process to synthesize a β-Bi_2O_3/Bi_2WO_6 nanocomposite using an ethylene glycol-based precursor solution. Apart from solvothermal processing, hydrothermal synthesis provides another useful route for controlling the formation and morphology of Bi_2O_3 nanostructures. Maestre & Santos [61] synthesized Bi_2O_3 NPs *via* a hydrothermal method, obtaining predominantly nanorod shaped particles with an average size of 150-250 nm.

Hydrothermal synthesis has been employed to prepare Bi_2O_3 based nanostructures and heterocomposites with improved functional properties. Raja *et al.* [64] synthesized a Bi_2O_3/ZnO heterostructure nanocomposite through this approach, establishing its applicability to the fabrication of semiconductor junctions. Mandawade *et al.* [63] reported flower-like Bi_2O_3 nanosheets with a hierarchical architecture, which exhibited photocatalytic activity towards methylene blue dye degradation and promising gas-sensing performance. Sayed *et al*. [60] developed a Bi_2O_3/Bi_2WO_6 heterojunction through an in situ hydrothermal-assisted impregnation method. The enhanced degradation of Indigo carmine was attributed to improved charge-carrier separation and strong interfacial interactions between the two semiconductor components.

Sonochemical method: Ultrasonic-assisted synthesis has emerged as a useful approach for controlling the particle size, morphology and dispersion of Bi_2O_3 nanostructures [65-69]. Its effectiveness is primarily related to acoustic cavitation, in which ultrasonic irradiation generates microscopic bubbles that undergo repeated growth and collapse within the reaction medium [70]. The collapse of these bubbles generates localized regions of high temperature and pressure, which promote rapid nucleation and crystal growth. These conditions facilitate nanoparticle formation without prolonged reaction periods or severe processing requirements. Kusuma *et al*. [68] prepared porous monoclinic Bi_2O_3 NPs with an average particle size of approximately 60 nm using a probe-assisted sonochemical process. Dinesh & Saranya [69] developed a green sono-chemical approach for synthesizing Bi_2O_3 NPs using *C. limon* extract as a natural stabilizing and capping agent. Under ultrasonic irradiation at 20 kHz, the extract-assisted process yielded rod-shaped nanostructures, which suggest that the combined influence of plant-derived constituents and acoustic cavitation can regulate particle growth and morphology.

Green synthesis method: Green synthesis offers an eco-friendly method to Bi_2O_3 NPs production through the use of biological resources such as plants, microorganisms, algae, fungi and agricultural waste [71-80]. Plant extracts are particularly useful due to their availability, low cost and abundance of bioactive compounds such as alkaloids, proteins, polyphenols, flavonoids and terpenoids. These phytochemicals participate in metal-ion conversion and regulate nanoparticle nucleation, growth and surface stabilization. The characteristics of the resulting Bi_2O_3 nanoparticles depend on the biological source, precursor concentration, solution pH, reaction temperature and synthesis duration [72-78]. Optimum conditions allows control over particle size, morphology, crystallinity and surface properties. The phytochemical residues adsorbed on nanoparticle surfaces can further improve colloidal stability and influence surface reactivity, with potential benefits for catalytic and photocatalytic applications [77-80].

Several studies have explored the use of biologically synthesized Bi_2O_3 for applications beyond conventional photocatalysis. Alam *et al.* [72] prepared nanocrystalline α-Bi_2O_3 through a bio-assisted combustion process using Mexican mint gel as an eco-friendly fuel. The resulting nanoparticles exhibited photocatalytic activity towards the degradation of Direct Green and Fast Orange Red dyes, along with electrochemical sensing capabilities for glucose and uric acid. Hamada *et al.* [77] employed olive leaf extract for the green synthesis of Bi_2O_3 NPs, which were subsequently incorporated into polyester composites for radiation shielding. Incorporation of 20 wt.% Bi_2O_3 improved gamma-ray attenuation and the thermal stability of the polymer matrix, extending the application of biogenic Bi_2O_3 to functional composite materials. Soundarya *et al*. [80] used *Datura innoxia* flower extract to prepare Bi_2O_3/$BiFeO_3$ nanocomposites through a green synthesis method. The resulting type-II heterojunction achieved 96.5% Rose Bengal dye removal under visible-light irradiation. The composite was further investigated for latent fingerprint visualization, which provide an additional application in forensic analysis. These findings establish the versatility of green-synthesized Bi_2O_3-based materials across environmental, electrochemical, radiation shielding and forensic applications.

Microwave assisted method: Microwave-assisted synthesis offers rapid and efficient heating through the interaction of microwave radiation with polar molecules and ionic species, accelerating nucleation and crystal growth [81]. This method reduces temperature gradients and processing time, enabling Bi_2O_3 nanostructure synthesis within minutes [82-88]. Reaction conditions, particularly irradiation time, precursor concentration and solvent composition, govern the resulting phase composition, particle size and morphology.

The influence of irradiation time on phase formation and morphology was examined by Sonkusare *et al*. [82], who synthesized Bi_2O_3 NPs from $Bi(NO_3)_3{\cdot}5H_2O$ using polyvinylpyrrolidone (PVP) and ethylene glycol. Irradiation for 10 min yielded flower-like α-Bi_2O_3 microstructures, whereas extending the treatment to 15 min resulted in the formation of spindle shaped γ-Bi_2O_3 NPs. This variation in morphology and crystal phase illustrates the sensitivity of microwave-assisted synthesis to reaction duration. Mohamed *et al.* [85] adopted microwave-assisted thermal treatment to prepare monoclinic α-Bi_2O_3

nanorods with an average length of ~101.5 nm. The synthesized nanorods exhibited photocatalytic activity towards bromocresol green degradation and antioxidant properties. The microwave irradiation has also been used to fabricate a layered BiOCl/BiOBr/Bi_2O_3 ternary heterojunction [86] for multicomponent photocatalytic applications.

Other synthesis methods: In addition to the commonly employed synthesis techniques discussed above, several alternative methods have been investigated for the fabrication of Bi_2O_3-based nanostructures. These methods offer different degrees of control over crystal structure, morphology and particle size depending on the intended application. Solution combustion synthesis involves a rapid self-sustaining exothermic reaction between metal precursors and fuel agents. The process enables the formation of highly porous Bi_2O_3 NPs within a short reaction time [88-91]. Murthy *et al*. [91] synthesized monoclinic Bi_2O_3 NPs using urea and lemon juice as combustion fuels. The resulting nanoparticles exhibited photocatalytic activity towards the degradation of acid orange-88, crystal violet and Rose Bengal under UV irradiation.

Solid-state reaction is a conventional high-temperature synthesis route based on the direct diffusion of solid precursors. It is suitable for large-scale preparation of highly crystalline Bi_2O_3, although control over particle size remains limited [92-95]. Tabassum *et al*. [93] prepared β-Bi_2O_3 nanocrystallites through the solid-state calcination of bismuth subcarbonate at 500 ºC. The resulting nanosheet-shaped photocatalyst achieved 91% degradation of ciprofloxacin under halogen lamp illumination. Its photocatalytic performance was attributed to the structural and morphological characteristics of the β-Bi_2O_3 nanocrystals.

Thermal decomposition involves the controlled pyrolysis of bismuth-containing compounds to obtain Bi_2O_3 with defined crystal phases and crystallinity [96-99]. Careful adjustment of the thermal treatment conditions provides an effective means of controlling Bi_2O_3 polymorphism. Li *et al*. [99] synthesized α-, β- and γ-Bi_2O_3 polymorphs by calcining flower-like $Bi_2O_2CO_3$ precursors previously prepared through a hydrothermal route. Heating at 400 ºC followed by natural cooling yielded α-Bi_2O_3, whereas controlled cooling at 5 ºC min^{-1} favoured the formation of the β-phase.

Pulsed laser ablation is a physical synthesis technique in which high-energy laser irradiation vaporizes a bismuth target to generate Bi_2O_3 nanoparticles without requiring chemical reducing agents [100-103]. Kamel *et al*. [100] synthesized α-Bi_2O_3 NPs through pulsed laser ablation and examined the influence of laser pulse energy on their structural and optical properties. Higher laser pulse energy improved nanoparticle crystallinity and optical response, which lead to enhanced photo-response in Bi_2O_3/porous silicon-based photodetectors.

Electrospinning is also widely used to fabricate 1D-Bi_2O_3 nanofibers with porous structures and interconnected networks that facilitate charge transport during photocatalytic processes [104-106]. Azman *et al*. [106] employed this method to fabricate ZnO/Bi_2O_3/epoxy–PVA composite nanofibers for radiation shielding applications. The resulting nanofiber mats exhibited improved attenuation of low-energy X-rays, supporting the use of Bi_2O_3 containing electrospun polymer composites in lightweight radiation shielding materials.

Microemulsion synthesis provides confined reaction environments through surfactant-stabilized droplets, enabling control over particle size, morphology and dispersion [107,108]. Wu *et al*. [108] incorporated La and Ce into the α-Bi_2O_3 lattice using reverse microemulsion synthesis followed by calcination at 500 ºC to improve photocatalytic performance. The microemulsion system consisted of cyclohexane, Triton X-100 and *n*-hexanol facilitated the formation of well-dispersed doped photocatalysts.

Spray pyrolysis involves the conversion of aerosolized precursor solutions into crystalline Bi_2O_3 powders or thin films through rapid thermal decomposition. Its scalability makes it suitable for industrial material production [109-111]. Jadhav *et al*. [110] prepared Bi_2O_3 thin films on glass substrates using an aqueous bismuth nitrate solution sprayed onto substrates maintained at 320 ºC. This process yielded porous polycrystalline Bi_2O_3 films.

Chemical vapour deposition (CVD) enables the growth of uniform Bi_2O_3 thin films with controlled composition and crystallinity. This technique is relevant to optoelectronic devices and photoelectrochemical and gas-sensing applications [112, 113]. Sun *et al*. [113] reported the CVD growth of metastable β-Bi_2O_3 on α-Al_2O_3 (0001) single-crystal substrates, yielding epitaxial thin films and particulate structures.

These synthesis routes provide additional options for controlling the structural and morphological characteristics of Bi_2O_3-based materials for environmental remediation, energy conversion and electronic applications. Table-1 summarizes the synthesis methods and reaction conditions reported for Bi_2O_3-based materials along with their resulting morphologies and the advantages and limitations of each approach.

Photocatalytic properties of Bi_2O_3 based nanostructures: In response to growing environmental pollution and increasing energy demands, semiconductor photocatalysts have received considerable attention for their ability to convert light energy into useful chemical transformations. Among visible light responsive semiconductors, Bi_2O_3 has emerged as a promising photocatalytic material owing to its favourable electronic structure, narrow band gap, chemical stability and polymorphic diversity [2-4]. Fig. 5 illustrates the principal photocatalytic characteristics of Bi_2O_3-based nanostructures under UV-visible light irradiation. Upon photoexcitation, electrons migrate from the valence band (VB) to the conduction band (CB), generating electron–hole pairs that participate in reactive oxygen species (ROS) formation. The conduction band electrons reduce dissolved oxygen to superoxide radicals ($^{\bullet}O_2^-$), while valence-band holes oxidize water or hydroxyl ions to generate hydroxyl radicals ($^{\bullet}OH$). These reactive species participate in the degradation and mineralization of organic contaminants into relatively harmless products such as CO_2, H_2O and inorganic ions. High surface area, efficient charge separation, chemical stability, broad pH tolerance and recyclability are important factors governing photocatalytic performance.

Unlike conventional photocatalysts such as TiO_2, which primarily absorb ultraviolet radiation, Bi_2O_3 can utilize visible light and access a substantial fraction of solar radiation [10]. This optical response makes it attractive for photocatalytic applications under natural sunlight. Its photocatalytic activity

TABLE-1
COMPARATIVE STUDY OF REPORTED Bi_2O_3 NANOSTRUCTURE SYNTHESIS CONDITIONS, MORPHOLOGY AND CHARACTERISTICS

Photocatalyst	Synthesis method	Reaction conditions	Morphology	Advantages	Limitations	Ref.
α, γ Bi_2O_3	Sol–gel	$Bi(NO_3)_3·5H_2O$ + citric acid (1:2 molar) + PEG 6000 in HNO_3; heated 90 ºC, aged for 12 h → gel; dried 100 ºC; calcined at 500, 600, or 700 ºC for 5 h	Irregular particles; SG500: 0.49-2.92 µm; SG600: 1.54-4.61 µm (whisker-like); SG700: 0.71-6.30 µm, coral-reef-like structure	Simple, low-cost route; calcination temperature alone tunes band gap and phase ratio; best photocatalytic rate (5.69 × 10^{-5} s^{-1} for methyl orange)	Less controlled particle size (micron-scale, not true nano); less phase purity	[43]
α-Bi_2O_3	Sol–gel	$Bi(NO_3)_3·5H_2O$ + citric acid + PEG600 in HNO_3: H_2O (1:5); pH adjusted to 3 with NaOH; sol heated 80 ºC for 3 h → gel; decomposed at 140 ºC	Spherical, crystallite size 32.47	Good dual pollutant degradation (dye & pesticide) -72% MB in 60 min; 67% chlorpyrifos in 60 min	Low degradation efficiency performance and highly pH-dependent,	[44]
Amorphous 1D Bi_2O_3 nanowires	Sol-gel + electrospinning	13% PAN in DMF + $Bi(NO_3)_3·5H_2O$; electrospun (flow 1.5 mL/h, 17 kV, 3.5 cm gap); calcined at 400ºC/600ºC for 3 h	1D nanowires, amorphous 150–500 nm	Defect-free 1D structure tunable refractive index (2.62→2.53), dielectric constant (6.87-6.42), for DSSC applications	Amorphous structure, sophisticated synthesis process (spin + vacuum calcination)	[46]
Bi_2O_3 (mixed α + γ phase)	Sol–gel (citric-acid route, calcination-time variation)	$Bi(NO_3)_3·5H_2O$ + citric acid (1:2) heated at 100 ºC for 20 h → gel; calcined at fixed 600 ºC for 1, 2, 3, 4, or 5 h	Coral-like, irregular particles with cavities, 1-8 µm	Photocatalytic rate 74.93% MO degradation), lower band gap (2.64/2.86 eV)	Micro size particles complicate the single band-gap assignment	[47]
α-Bi_2O_3, β-Bi_2O_3	Co-precipitation (CP) *vs.* sol–gel (SG)	CP: $Bi(NO_3)_3·5H_2O$ + NaOH, pH 11, 75 ºC/2 h, calcined 450 ºC/2 h. SG: $Bi(CH_3COO)_3$ + oxalic acid (1:2 molar), pH 2 (HCl), dried 80 ºC, calcined 400 ºC/2 h	CP: rod-shaped, non-uniform, crystallite 41 nmSG: flower- and needle-like, crystallite 31 nm	Complete paracetamol degradation in just 15 min under sunlight 90 min for CP; 99.19% TOC removal	CP is simpler/cheaper but much slower and less complete (60–90 min)	[48]
Zn^{2+}-α-Bi_2O_3	Citrate sol–gel (auto-combustion)	$Bi(NO_3)_3·5H_2O$ + citric acid (equimolar) in HNO_3, + $Zn(NO_3)_2·6H_2O$ at 0, 1.5, 3, 4.5 vol%; heated 100 ºC, auto combustion to foam, calcined 600 ºC/2 h	Plate-like structure, crystallite size 40–51 nm;	Good conductivity 2.19 × 10^{-5} S/cm) and mobility (6.89 $cm^2/V·s$); MB dye degradation (~95%), good stability	Doping causes particle aggregation	[49]
α-Bi_2O_3	Precipitation method	$Bi(NO_3)_3·5H_2O$ + chitosan (Cs)/sodium alginate (Alg) + NaOH → precipitation; drying at 100 ºC → calcination at 400 ºC for 4 h.	Chitosan-containing α-Bi_2O_3 exhibits elongated structures, alginate-containing α-Bi_2O_3 irregular and aggregated	90% AO7 removal at pH 6.31 without additional pH adjustment; activity under both UV-B and visible light; good stability.	Stronger particle agglomeration is observed; Calcination is still required to obtain catalyst. photocatalytic performance is sensitive to the choice of templating agent.	[50]
α-Bi_2O_3 needles	Co-precipitation	$Bi(NO_3)_3·5H_2O$ dissolved in 2 M HNO_3, stirred 90 min at 75 ºC; 2 M NaOH added dropwise until pH 12 → pale-yellow precipitate; dried at 80 ºC; annealed 2 h at 200-700 ºC	Needle-shaped crystals, crystallite size 43-82 nm	Degradation efficiency (98%) µm (700 ºC); crystallite size 43–82 nm	Higher annealing temperature reduces photocatalytic the better crystallinity shows a limitation in photocatalyst activity	[51]
α-Bi_2O_3	Co-precipitation (formic acid + pectin)	0.8 g $Bi(NO_3)_3·5H_2O$ + 10 mL formic acid containing 50 mg pectin (dried by microwave; annealed 100–400 ºC (5 h) — 250 ºC	Fibre-like morphology: length 0.2-3.2 µm, cross-section 0.05–0.18 µm	Clear morphology with good gas sensing properties	Requires careful annealing-temperature control to hit the desired α-phase; NO_2 gas released during synthesis, gas sensor needs elevated operating temperature (300 ºC)	[52]
Bi_2O_3-MgO-GO	Co-precipitation (onto pre-made GO)	GO (Hummers' method) sonicated in DI water; $Bi(NO_3)_3·5H_2O$ + $Mg(NO_3)_2·6H_2O$ (0.1 M each) mixed with GO dispersion; heated 70 ºC, annealed 150 ºC/2 h	Crystallite size 28.06 nm (XRD)	Good zeta potential = 48.0 mV, UVC emissive devices	Very large band gap limits visible-light photocatalytic use; the two techniques (PL *vs.* UV-vis) give notably different band-gap values, attributed to defects/impurities	[53]
β-Bi_2O_3 – Bi_2WO_4	Two-step solvothermal + calcination	(Bi_2WO_4): $Bi(NO_3)_3·5H_2O$ + $Na_2WO_4·2H_2O$ in ethylene glycol, autoclaved 180 ºC/15 h, calcined 300 ºC/3 hr. (β-Bi_2O_3 deposition)	Bi_2WO_4 =28.39 nm nm, β-Bi_2O_3 - Bi_2WO_4 = 21 nm	Good photocurrent density and photovoltage achieved 6.42 mA/cm^2 and -0.35V, MO and RhB dye degradation achieved 75% and 80%	Requires (more time, energy as compare to single-step routes); β-Bi_2O_3 diffraction peaks nearly overlap with Bi_2WO_4 peaks in XRD,	[57]

Bi_2O_3/Bi_2WO_6 nanocomposite	*In situ* hydrothermal	Bi_2O_3:WO_3 = 1.5:1 molar ratio; $Bi(NO_3)_3·5H_2O$ + WO_3+ urea; 160 ºC, 24 h; dried at 100 ºC, 24 h; calcined at 500 ºC, 2 h	Crystallite size: 6.88–31.22 nm; avg. 18.10 nm; nano-flakes; hierarchical flower-like structure	Visible-light active; enhanced charge separation; IC degradation ~100%/120 min; mineralization 88.9%; stable for 4 cycles	Long hydrothermal treatment (24 h); calcination required; particle agglomeration; relatively high catalyst loading (1.5 g/L); visible-light rate lower than UV-A	[60]
Bi_2O_3 nanoflakes	Sol–gel	$Bi(NO_3)_3·5H_2O$ 0.1 M/50 mL + PEG 600 (5 mL); stirring 450 rpm/1 h; dried 80 ºC/5 h; calcined 500 ºC/30 min	Crystallite size: ~15 nm; TEM particle size: 28.50 nm; hierarchical nanoflakes; porous structure	Higher MB degradation (95.73%/120 min); higher rate constant (0.02706 min^{-1}); good sunlight response; higher surface area and porosity; H_2S sensing	Sunlight dependent; MB only; 120 min irradiation; no reusability study reported	[63]
Bi_2O_3 nanosheets	Hydrothermal	$Bi(NO_3)_3·5H_2O$ 0.2 M/50 mL; HNO_3; 1 M NaOH for pH adjustment; 180 ºC/18 h; dried 120 ºC; calcined 500 ºC	Crystallite size: ~16 nm; TEM particle size: 60.56 nm; nanosheet/flower-like one-sided arrangement	High crystallinity; sunlight-driven MB degradation (90.22%/120 min)	Low rate constant, long reaction time, larger size	
Bi_2O_3/ZnO heterostructure nanocomposite	Hydrothermal technique	Optimized at pH 7–9, catalyst dose 9 mg, dye concentration 10 ppm; UV irradiation	Crystallite size: ~12 nm; Band gap = 2.78 eV	Enhanced photocatalytic activity; MG: 95%/180 min; AB113: 92%/240 min	UV-light dependent; relatively long irradiation time; optimization required for pH and catalyst dosage;	[64]
Bi_2O_3 nanoparticles	Probe sonication/ sonochemical	$Bi(NO_3)_3·5H_2O$ + NaOH (1:2); HNO_3 + DI water; 40 ºC, 1 h; ultrasonic probe 20 kHz, 20% amplitude; dried 100 ºC/1 h; calcined 600 ºC/2 h	Crystallite size: 58.79 nm; monoclinic α-Bi_2O_3; highly porous, irregular; sheet-like morphology	Simple, low-cost and rapid sonochemical synthesis; MB 93.45% and AR 97.80% degradation	Wide band gap (3.3 eV); mainly UV-responsive; agglomeration; 60 mg catalyst/250 mL dye solution; no visible-light advantage demonstrated	[68]
α-Bi_2O_3 nanoparticles	Green sonochemical/ sono-cavitation using *Citrus limon* extract	Bi oxynitrate 0.05 M/100 mL + lemon extract; stirred 60 min; sonication 20 kHz, 30 min; probe 13 mm; dried 105 ºC/24 h	crystallite size: 26 nm; SEM: nano short-rod or facet-like structures	Simple, low-cost synthesis; lemon extract acts as reducing with capping agent; CR degradation ~86%/30 min; stable over 4 cycles	High catalyst loading; degradation decreases at high dye concentration; particle aggregation at excessive catalyst loading	[69]
α-Bi_2O_3 nanoparticles	Green solution-combustion using Mexican mint gel	5 g Mexican mint leaves + 10 mL DD water; stirred 30 min; 10 mL extract used as fuel + stoichiometric Bi nitrate; 250 ºC/2 h combustion; calcined 600 ºC/2 h	XRD crystallite size: ~60 nm; TEM: <55 nm; spherical nanoparticles; crystalline SAED pattern	Simple, low-temperature combustion; plant-derived fuel; α-phase Bi_2O_3; photocatalytic dye degradation + glucose/uric-acid sensing	UV-dependent higher activity; relatively large nanoparticles; agglomeration tendency; limited dye concentration range; acidic electrolyte required for sensing	[72]
Bi_2O_3 NPs/Unsaturated polyester nanocomposite	Green synthesis using olive-leaf extract	Bi precursor + olive-leaf extract; stirring 3 h → 70 ºC/4 h drying → 600 ºC/2 h calcination	TEM particle size: ~15 nm; Bi_2O_3 nanoparticles dispersed in polyester	Eco-friendly synthesis; lead-free shielding; improved gamma attenuation; improved thermal stability	Compressive strength decreases with Bi_2O_3 loading; mainly effective for low-energy photons; attenuation decreases with increasing photon energy	[77]
α-Bi_2O_3 γ-Bi_2O_3	Microwave-assisted synthesis	$Bi(NO_3)_3·5H_2O$ + PVP; MW irradiation: 10 min and 15 min	Monoclinic α-Bi_2O_3; microflower architecture; HR-TEM: nanoflakes 19–35 nm Cubic/bcc γ-Bi_2O_3; microspindle architecture; HR-TEM: 15–30 nm	Enhanced UV photocatalysis; degradation of 5 dyes; pseudo first order kinetics; stable up to 4 cycles	UV-light dependent; Lower photocatalytic and antibacterial performance than α-Bi_2O_3 MFs; UV-dependent	[82]

is strongly influenced by the valence and conduction band positions, which govern light absorption and interfacial redox reactions. Depending on the crystal polymorph, Bi_2O_3 exhibits a direct optical band gap of approximately 2.3-2.8 eV, which enable the absorption across a considerable portion of the visible spectrum. Photons with energy equal to or higher than the band gap excite electrons from the valence band to the conduction band and generate corresponding holes in the valence band [10]. These charge carriers migrate towards the catalyst surface and participate in reduction and oxidation reactions through the formation of $^{\bullet}O_2^-$ and $^{\bullet}OH$ radicals. Direct oxidation by photogenerated holes further contributes to contaminant degradation and mineralization into CO_2, H_2O and other inorganic products [3,4].

Despite its favourable optical properties, pristine Bi_2O_3 suffers from several limitations that restrict its photocatalytic

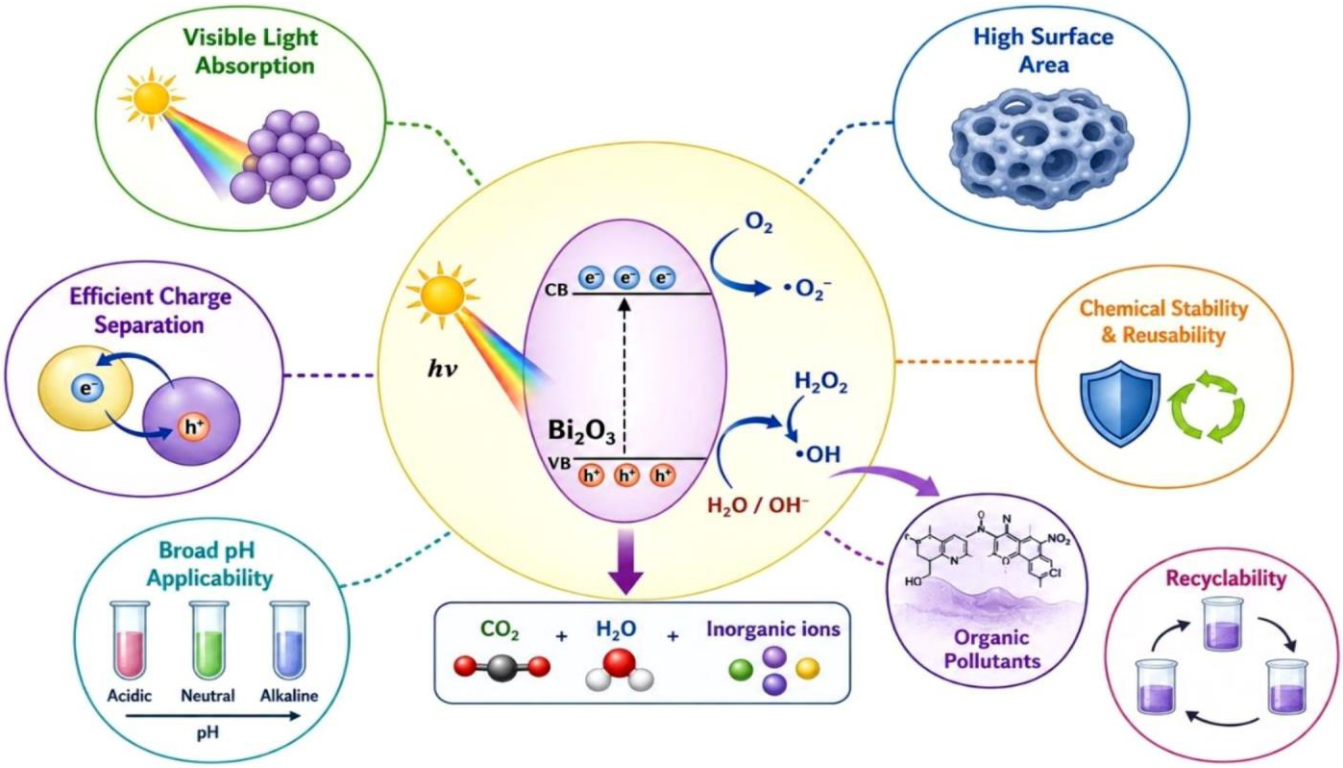


Fig. 5. Schematic diagram showing the key photocatalytic characteristics of Bi_2O_3 nanostructures under the irradiation of UV-Vis light

efficiency under practical operating conditions. Rapid recombination of photogenerated charge carriers, limited utilization of incident photons, susceptibility to photocorrosion during prolonged irradiation and inadequate redox capability remain major challenges [5-8]. Extensive research has focused on modifying the physicochemical properties of Bi_2O_3 through elemental doping, defect engineering, morphology control, noble metal decouration and semiconductor heterostructure fabrication [4]. These modifications regulate its electronic structure and interfacial charge-transfer characteristics. The construction of p–n junctions, type-II heterojunctions, Z-scheme and S-scheme architectures has received particular attention for improving charge separation and visible-light absorption while maintaining suitable redox potentials. Such structural modifications offer an effective route towards improving the photocatalytic degradation of environmental pollutants.

Photocatalytic degradation of organic pollutants

Pure Bi_2O_3: The photocatalytic properties of Bi_2O_3 can be tailored by controlling its crystal phase, morphology, crystallinity and surface characteristics through suitable synthesis methods [7,10]. Intrinsic parameters such as particle size, exposed crystal facets and oxygen-vacancy concentration further influence its catalytic behaviour [7]. Nanoscale structures such as nanoparticles, nanorods, nanowires, nanosheets and hierarchical flower-like architectures offer improved surface accessibility and can enhance photocatalytic reactions. Under visible-light irradiation, electrons are excited from the valence band to the conduction band, leaving behind holes in the valence band [4]. Fig. 6 illustrates the photocatalytic mechanism and band alignment of pristine Bi_2O_3. Several studies have reported the degradation of organic dyes, pharmaceutical contaminants, pesticides and phenolic compounds using pure Bi_2O_3 under visible-light and solar irradiation [2-4,7,10].

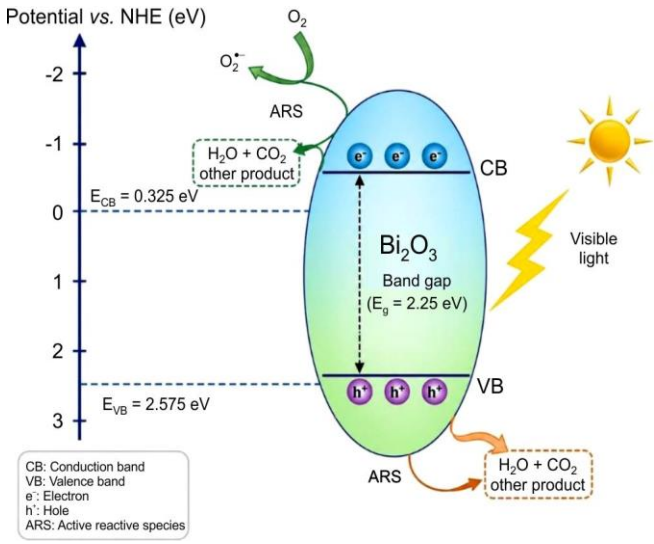


Fig. 6. Band diagram showing photocatalytic process in Bi_2O_3

Aksit *et al.* [48] compared co-precipitated and sol-gel derived tetragonal Bi_2O_3 for the degradation of 25 mg L^{-1} paracetamol under UVA, UVB, UVC and solar irradiation. The Bi_2O_3-SG (1:2) catalyst achieved 100% degradation within 15 min under UVB and 99.5% within 30 min under direct sunlight. Its maximum degradation rate constant reached 0.321 min^{-1}. At pH 5, the complete degradation of paracetamol required 60 min compared with 90 min for the co-precipitated sample under identical conditions. The improved activity was

attributed to the lower band gap, higher specific surface area, abundant surface hydroxyl groups and improved charge separation. The catalyst further achieved 99.19% TOC removal within 60 min, indicating extensive mineralization of paracetamol into CO_2 and H_2O.

Janardhana *et al*. [26] investigated β-Bi_2O_3 nanoparticles obtained through ball-milling-induced phase transformation of α-Bi_2O_3 for the degradation of RhB dye (5 mg L^{-1}) under UV-visible (250 W) and simulated solar irradiation (400-1100 nm). Compared with needle-like α-Bi_2O_3, petal-shaped β-Bi_2O_3 exhibited a lower band gap (2.5 *vs*. 2.9 eV), higher specific surface area (3.61 *vs*. 1.38 m^2 g^{-1}), larger pore diameter (1.07 nm) and higher oxygen-vacancy concentration. These characteristics favoured visible-light absorption and charge separation. The β-phase achieved 97% RhB degradation within 75 min under UV-visible irradiation with a pseudo-first-order rate constant of 48.1 × 10^{-3} min^{-1}. Under identical conditions α-Bi_2O_3 achieved only 55% degradation with a rate constant of 8.7 × 10^{-3} min^{-1}. Under simulated solar irradiation β-Bi_2O_3 retained 91% degradation efficiency after 150 min with a rate constant of 17.1 × 10^{-3} min^{-1}, whereas α-Bi_2O_3 achieved 30% degradation with a rate constant of 2.3 × 10^{-3} min^{-1}. The superior activity of β-Bi_2O_3 was linked to its enhanced optical absorption up to 540 nm, higher adsorption capacity (30% compared with 20% for β-Bi_2O_3 in the dark) and reduced electron–hole recombination. Band-edge analysis yielded CB and VB potentials of 0.48 and 2.98 eV for β-Bi_2O_3. These values point to a photocatalytic pathway dominated by hole-induced hydroxyl radical formation and dye sensitization.

Meher *et al*. [39] reported the photocatalytic degradation of brilliant green dye using sol-gel derived monoclinic α-Bi_2O_3 nanoparticles. The catalyst achieved 93.25% dye mineralization within 180 min at an optimized photocatalyst dosage of 7.5 mg L^{-1}. Oxygen vacancies (V_o) played an important role in interfacial charge transfer and suppression of electron–hole recombination. Improved ROS generation through $^{\bullet}OH$ and $^{\bullet}O_2^-$ formation contributed to the oxidative degradation of the dye.

Several other studies have investigated pristine Bi_2O_3 for the degradation and mineralization of dyes, antibiotics, pharmaceutical compounds, pesticides, phenolic compounds and endocrine-disrupting chemicals under UV and visible-light irradiation [2-4,10,43,44,50-52,63,73,75,76,82,83,85,91,111,114-117]. The reported findings establish crystal phase, morphology, oxygen vacancies and surface characteristics as key factors governing photocatalytic performance. Table-2 summarizes the photocatalytic dye-degradation performance of pure and modified Bi_2O_3 nanostructures.

Doped Bi_2O_3: Elemental doping is a widely adopted strategy for improving the photocatalytic properties of Bi_2O_3 through controlled modification of its electronic structure and surface chemistry [16,49,54,94,108,118-126]. Dopant incorporation can introduce intermediate energy levels, modify the band-gap energy, promote oxygen-vacancy formation and improve the separation of photogenerated electron–hole pairs. These changes can enhance visible-light absorption and reduce charge-carrier recombination, which lead to the improved photocatalytic activity (Fig. 7). Khan *et al*. [49] synthesized Zn^{2+}-doped α-Bi_2O_3 through a citrate-assisted sol-gel method and investigated its photocatalytic degradation of methylene blue dye under solar irradiation. Among the investigated compositions, 4.5% Zn^{2+} doping achieved the highest degradation efficiency of nearly 95% within 140 min. The pseudo-first-order rate constant increased from 0.018 min^{-1} for pristine Bi_2O_3 to 0.039 min^{-1} for the optimally doped sample. Zn incorporation improved electrical conductivity to 2.79 ×

TABLE-2
COMPARATIVE PHOTOCATALYTIC PERFORMANCE OF PRISTINE AND MODIFIED Bi_2O_3 NANOSTRUCTURES TOWARD ORGANIC DYES

Photocatalyst	Pollutant	Conc.	Catalyst dosage (mg/L)	Light source	Irradiation time	Degradation efficiency	Ref
Zeolite/Bi_2O_3	RhB dye	50 mg/L	550 mg/L	Adsorption study: Digital orbital shaker set at 260rpm, 25 ºC with contact time 20-60 min	60 min	98.12%	[9]
NiO/Bi_2O_3/Bi_3ClO_4	Acid red 88	10 mg/L	800 mg/L	visible light (λ > 400 nm) irradiation	120 min	89%	[12]
Bi_2O_3–TiO_2	MO and MB	30mg/L	666 mg/L	10W UVA lamp	120 min	93.9% and 98.2%	[21]
Bi_2O_3	Crystal violet	30mg/L	333 mg/L	Visible light sodium lamp 250-W	80 min	99.88 %	[25]
4.5% Zn^{2+}- α-Bi_2O_3 (ZBO-D)	Methylene blue (MB)	1 mg/L	200 mg	Natural sunlight, 950 ± 25 W/m^2	140 min	95%	[49]
Bi/Bi_2O_3 -TiO_2	RhB, MO dye	0.02 mg/L	Immobilized film electrode, 1.8 cm^2	500 W Xe lamp (CEL-S500), +1 V bias, PEC mode	180 min	80%, 18% (PC only, *vs*. 75% under PEC bias)	[56]
β-Bi_2O_3 Bi_2WO_6	Ciprofloxacin	15 mg/L	100mg/L	300 W Xe lamp, visible light	90 min	~92.91%	[57]
Bi_2O_3 NPs	Methylene blue, Acid red dye	20 mg/L	240 mg/L	UV light - Hg vapour lamp, 125 W medium pressure, λ_{max} ≈ 370 nm (UVA)	120 min	93.45%, 97.80%	[68]
Bi_2O_3	Congo red	20 mg/L	120 mg/L	(Ultrasonic probe 500 W, frequency 20 kHz	30 min	86%	[69]
Bi_2O_3	Crystal violet (CV)	30 mg/L	20 mg (in 60 mL dye solution)	Visible light -250 W Na lamp	110 min total	99.88% (highest of the series)	[73]
α-Bi_2O_3	Bromocresol green (BG)	20 mg/L	0.075 g (75 mg) at optimum pH 6	UV/visible - 250 W Xe discharge lamp	180 min (3 h)	~75% (74.5%)	[85]

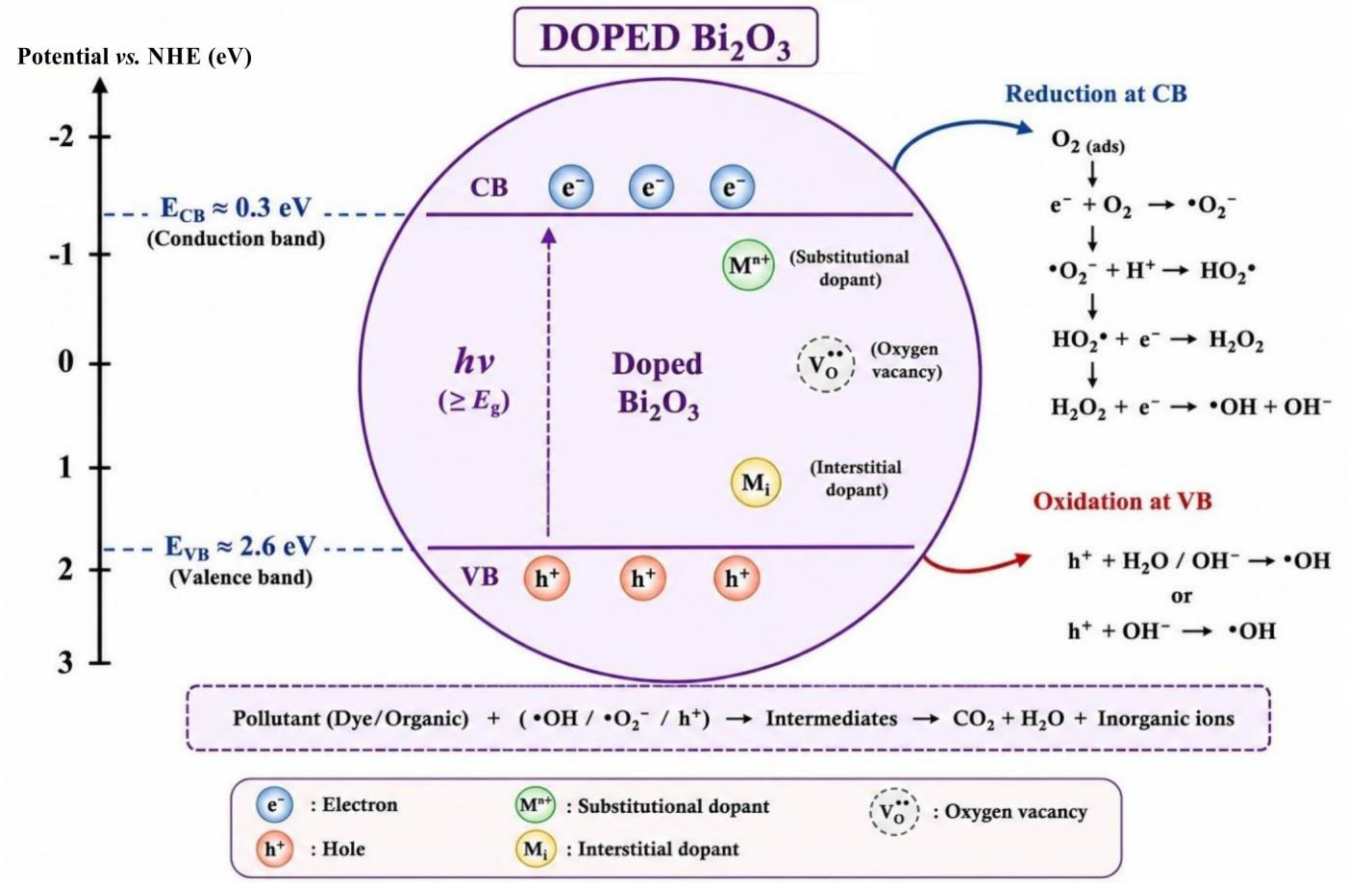


Fig. 7. Band diagram showing photocatalytic process in doped Bi_2O_3

10^{-5} S cm^{-1} and carrier mobility to 6.89 cm^{-2} V^{-1} s^{-1}. These changes favoured electron trapping and de-trapping while limiting charge recombination. Scavenger experiments identified •OH radicals as the dominant reactive species. The photocatalyst retained good stability with only a 3.1% reduction in activity after three recycling cycles.

Viruthagiri & Kannan [123] synthesized Co-doped α-Bi_2O_3 nanoparticles through a precipitation method and investigated their photocatalytic activity towards MB degradation. The optimum Co doping concentration of 3% achieved 97% degradation within 135 min compared with 76.15% for pristine Bi_2O_3. The improved activity was attributed to better charge-carrier separation and increased dye adsorption along with enhanced visible-light absorption. The photocatalytic degradation involved the generation of •OH and $•O_2^-$ radicals which facilitated the oxidative breakdown of methylene blue (MB) molecules into colourless products.

Sharaf *et al.* [126] reported enhanced photocatalytic activity in Mg-doped β-Bi_2O_3 synthesized through a sol–gel method. Mg incorporation reduced the crystallite size from 79 to 13 nm and narrowed the band gap from 3.8 to 3.08-3.30 eV. A shift in the valence-band potential from 3.37 to 2.78-2.91 V was observed with a value of 3.2 V reported for $Mg_{0.075}Bi_{1.925}O_3$. The sample containing 0.1 M Mg exhibited the highest pseudo-first-order rate constant of 0.0217 min^{-1}. Its improved photocatalytic performance was attributed to enhanced visible-light absorption and charge separation.

Prakash *et al.* [124] synthesized Ag-doped Bi_2O_3 nanoparticles through a green sol-gel route using *Coldenia procumbens* leaf extract. The Ag-doped samples exhibited improved visible-light-driven MB degradation with photocatalytic activity strongly dependent on the Ag concentration. The synthesized nanoparticles were also evaluated for antibacterial and larvicidal applications. Similar improvements in photocatalytic activity have been reported for other doped Bi_2O_3 systems [118-126]. These studies establish dopant concentration and chemical composition as important parameters governing the structural and optoelectronic properties of Bi_2O_3. Table-3 summarizes the effects of different dopants on the structural, optical and photocatalytic properties of Bi_2O_3.

Bi_2O_3-based heterostructures: Semiconductor heterojunction fabrication is an effective approach for overcoming the inherent limitations of pristine Bi_2O_3 and improving its photocatalytic performance [2-4]. Coupling Bi_2O_3 with semiconductors possessing suitable band-edge positions facilitates the separation and migration of photogenerated charge carriers while extending visible-light absorption [3,4]. Interfacial charge transfer reduces electron–hole recombination and can preserve the oxidation and reduction capabilities required for photocatalytic reactions. These characteristics have encouraged the development of Bi_2O_3-based heterostructures for the degradation of persistent organic pollutants and emerging contaminants in wastewater. Depending on the relative band-edge positions of the constituent semiconductors, diff-

TABLE-3
EFFECT OF DOPANTS ON THE STRUCTURAL, OPTICAL AND PHOTOCATALYTIC PROPERTIES OF Bi_2O_3

Pristine material	Dopant	Structural change	Band-gap change	Photocatalytic efficiency	Ref.
Bi_2O_3	None	δ-Bi_2O_3 (FCC, fluorite), spherical NPs 10–20 nm, mesoporous, SBET = 71 m^2/g	Band gap = 3.45 eV	98.26% Thymol Blue degraded; 69.67% Congo Red degraded	[117]
Bi_2O_3	La^{3+}	(2% La: 12.6 m^2/g *vs.* 2.54 m^2/g undoped)	Bi_2O_3 2.853 eV → 1% La 2.855 → 2% La 2.849 → 3% La 2.838 eV	98% methyl MO degraded (100 min); 73% phenol degraded (4 h)	[118]
Bi_2O_3	Li + Co	Bi_2O_3 + $LiBiO_3$ nanoplates (50–150 nm thick)	Band gap ↓: $LiBi_2O_3$ nanoplates 1.52 eV → $CoLiBi_2O_3$ hybrids 1.25 eV	100% degradation of Gentian Violet in 60 min (UV–vis light); $LiBi_2O_3$ alone 99.7% in 360 min	[119]
Bi_2O_3	Ce^{3+}	α-Bi_2O_3 retained; hollow needle-shape morphology; HNB-Ce-5 SBET = 149.51 m^2/g	Band gap order: CNB > HNB > HNB-Ce-7 > HNB-Ce-3 > HNB-Ce-5 (Ce doping reduces gap; exact eV not reported)	HNB-Ce-5: 89.1% tetracycline degraded (300 W visible light) *vs.* 71.4% (HNB) and 37.0% (commercial Bi_2O_3)	[120]
Bi_2O_3	Fe	Bi_2O_3 . (26 nm) → Fe Bi_2O_3-(32 nm), needle→plate/polyhedral morphology shift	--	99% Basic Brown 1 dye removal (42 min); real textile wastewater 77%	[121]
Bi_2O_3	Ni	δ-Bi_2O_3 -30-60 nm, Ni-Bi_2O_3 300 to 1000 nm	Bi_2O_3 2.87 eV → Ni-Bi_2O_3-2 2.58 eV → Ni-Bi_2O_3-5 2.49 eV	Ni-Bi_2O_3 52.2% degradation, Bi_2O_3 31.1% (undoped) under simulated solar light	[122]
Bi_2O_3	Ce^{3+}	α-Bi_2O_3 54.43 nm, Ce-Bi_2O_3 0.62 nm	Bi_2O_3 =2.643 eV, 0.15 M Ce-Bi_2O_3 = 2.045 eV 0.25 M Co-Bi_2O_3 = 1.9424 eV	0.15 M Co-Bi_2O_3: 97% (MB dye) degradation *vs.* 76.15% (pure Bi_2O_3)	[123]
Bi_2O_3	MoS_2 nanosheets	BET surface area: Bi_2O_3 8.5, MoS_2/Bi_2O_3 185 $m^2/gMoS_2/Bi_2O_3$	Bi_2O_3 = 2.82 eV; MoS_2 = 1.9 eV	15% MoS_2/Bi_2O_3=89.6% 2-mercaptobenzothiazole, 79.3% tetracycline and 90% RhB removal	[127]
Bi_2O_3	*g*-C_3N_4 support with α-Bi_2O_3 loading	BET SA of 1 wt.% composite (17.1 m^2/g) *g*-C_3N_4 (18.1 m^2/g)	*g*-C_3N_4 = 2.72 eV; 0.5 wt.%=2.70, 1 wt.%=2.69, 3 wt.%=2.66, 5 wt.%=2.64 eV; pure α-Bi_2O_3: 2.80 eV	1 wt.% α-Bi_2O_3 -*g*-C_3N_4 =92% BP-3 degradation	[128]
Bi_2O_3	Reduced graphene oxide (RGO)	α-Bi_2O_3/RGO average particle size 12 nm	--	90 min: 52.89% Methylene blue, 41.50% Alizarin yellow, 32.51% Lissamine green	[129]
Bi_2O_3	Carbon quantum dots	Carbon quantum dots, sono-chemical, template-free	C-dots/Bi_2O_3 28.75 nm	α-Bi_2O_3 : 2.7 eV → α-Bi_2O_3/C-dots: 2.49 eV (redshift)	[130]
Bi_2O_3	Porous *g*-C_3N_4 support with -Bi_2O_3loading	Porous *g*-C_3N_4 support with -Bi_2O_3 loading (3, 6, 9, 12, 15 wt.%; optimum 9 wt.%) — direct Z-scheme	Bi_2O_3 particles decorate porous *g*-C_3N_4 sheets	Porous *g*-C_3N_4: 2.82 eV; Bi_2O_3:2.80 eV	[131]

erent charge-transfer mechanisms can operate within these systems. The major configurations include type-II heterojunctions, p–n junctions, Schottky junctions, Z-scheme and S-scheme architectures (Fig. 8) [2-4,10]. Each configuration offers a distinct pathway for charge-carrier migration and influences the redox potential and photocatalytic activity of the resulting composite. Recent studies [11,12,19,21,22,26,27,45,53,56,60,64,67,78-80,84,86,101,106,127-138] have reported improved photocatalytic degradation through the integration of Bi_2O_3 with TiO_2, ZnO, CuO, MnO_2, Fe_2O_3, WO_3, *g*-C_3N_4, BiOCl, MgO, CdS, Bi_2S_3, Bi_2WO_6, graphene derivatives, MXenes and metal-organic frameworks (MOFs). These combinations provide opportunities to regulate interfacial charge transport and improve the photocatalytic degradation of environmental contaminants.

Ruiz-Santoyo *et al.* [21] synthesized TiO_2/Bi_2O_3 heterostructures through a hydrothermal method and investigated their photocatalytic activity towards methyl orange (MO) and methylene blue (MB) degradation. The BiT16 sample achieved 93.9% MO and 98.2% MB degradation within 120 min. The degradation followed pseudo-first-order kinetics with rate constants of 0.03768 and 0.04214 min^{-1} for MO and MB respectively. The improved activity was attributed to the formation of a TiO_2/Bi_2O_3 p–n heterojunction that facilitated charge separation and reduced electron–hole recombination. The catalyst achieved COD removal efficiencies of 91.5% for MO and 94.3% for MB. It retained 65.6% and 70.5% of its initial photocatalytic activity towards MO and MB respectively after three reuse cycles.

Meher *et al*. [22] fabricated a ZnO/Bi_2O_3 heterojunction through a sonochemical method. The composite achieved 93.24% MB and 92.47% Congo red (CR) degradation within 180 min. Its improved photocatalytic activity was attributed to efficient electron–hole separation at the ZnO/Bi_2O_3 interface and enhanced $^{\bullet}OH$ radical generation. The catalyst exhibited good reusability during repeated photocatalytic cycles.

Fan *et al*. [32] developed a Z-scheme Bi_2O_3/g-C_3N_4 heterojunction through *in situ* thermal polymerization. The composite achieved complete MB degradation within 90 min. Its enhanced photocatalytic activity was attributed to efficient charge-carrier separation across the Z-scheme interface. Hydroxyl radicals ($^{\bullet}OH$) were identified as the dominant reactive species while $^{\bullet}O_2^-$ radicals and photogenerated electrons and holes played secondary roles in the degradation process.

Xie *et al.* [33] constructed a 0D/2D Z-scheme TiO_2/Bi_2O_3 heterojunction. The optimized TB-3 photocatalyst containing 15 wt.% TiO_2/Bi_2O_3 exhibited the highest visible-light-driven degradation of tetracycline hydrochloride (TC). The Z-scheme architecture facilitated charge-carrier migra-

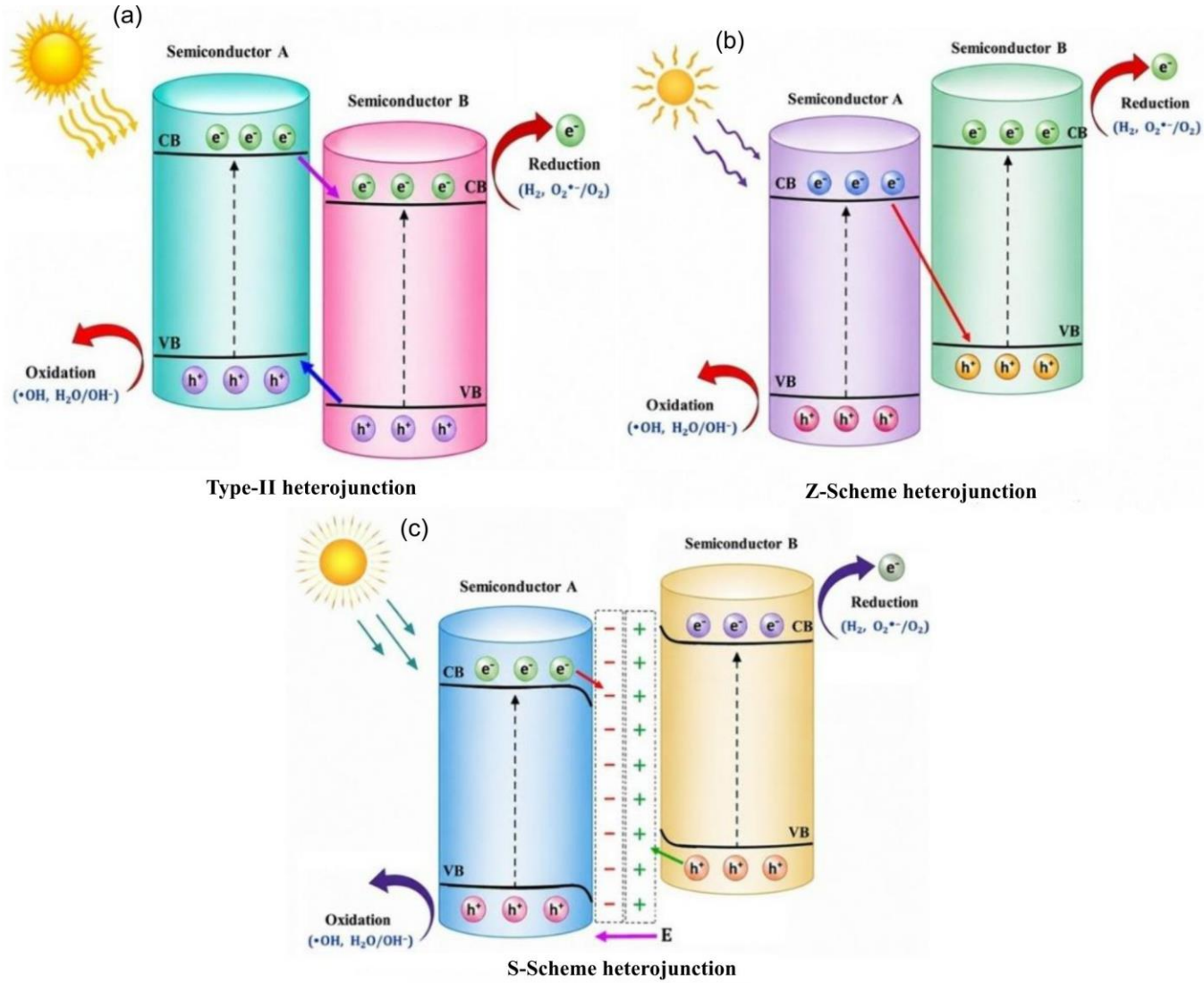


Fig. 8. Band diagram for (a) Type-II, (b) Z-scheme and (c) S-scheme heterojunctions showing photocatalytic process

tion while preserving strong redox potentials. Enhanced visible light absorption and superoxide radical ($^{\bullet}O_2^-$) generation contributed to the degradation process. Sayed *et al.* [60] synthesized Bi_2O_3/Bi_2WO_6 heterojunction nanocomposites through an in situ hydrothermal-assisted impregnation method. The composites exhibited improved visible-light-driven degradation of indigo carmine (IC) under irradiation at wavelengths above 350 nm compared with pristine Bi_2O_3 and Bi_2WO_6. Improved interfacial charge separation was supported by photoluminescence and radical-trapping experiments. The composite retained good photocatalytic stability and recyclability during repeated use.

Raja *et al.* [64] reported hydrothermally synthesized Bi_2O_3/ZnO nanocomposites with improved photocatalytic activity under UV irradiation. The composite achieved 95% degradation of malachite green (MG) within 180 min and 92% degradation of acid blue 113 (AB113) within 240 min. The improved performance was attributed to heterojunction formation and favourable structural characteristics. The composite exhibited crystallite sizes of ~12 nm and a narrowed band gap of 2.78 eV. The good photocatalytic reusability was retained after three successive cycles. Chavan *et al.* [132] investigated MnO_2-based nanocomposites containing 5% Zn-doped β-Bi_2O_3 for sunlight-driven photocatalysis. The optimized composite achieved 92.4% MB and 99.5% rhodamine B (RhB) degradation. Its improved activity was associated with a reduced particle size of 8.61 nm and a narrowed band gap of 2.61 eV along with improved charge-carrier separation.

The growing range of Bi_2O_3-based heterostructures reported in the literature establishes their potential for the photocatalytic degradation of dyes, antibiotics and other organic contaminants. These composites have further attracted interest in hydrogen generation and antimicrobial applications [128-138]. Table-4 summarizes the photocatalytic mechanisms and experimental conditions reported for Bi_2O_3-based heterostructures during pollutant degradation.

Mechanism of photocatalytic dye degradation: The photocatalytic activity of Bi_2O_3-based nanomaterials involves light-induced electronic excitation followed by surface redox reactions. Upon irradiation with photons possessing energy equal to or higher than the band gap (E_g), electrons migrate from the valence band to the conduction band, leaving posi-

TABLE-4
PHOTOCATALYTIC MECHANISM IN Bi_2O_3-BASED HETEROJUNCTIONS FOR DYE DEGRADATION

Bi_2O_3-based heterojunction	Pollutant	Light source	Degradation efficiency	Proposed charge transfer mechanism	Ref.
ZnO/Bi_2O_3	Methylene blue (MB) and Congo red (CR) dyes	55 W DULUX UV-Vis lamp	93.24% and 92.47% 180 min	Type-II heterojunction	[22]
0D/2D TiO_2NPs/Bi_2O_3	Tetracycline hydrochloride (TC) antibiotic (+ H_2 evolution)	300 W xenon lamp with 420 nm cut-off filter (visible light)	65–80%, H_2 evolution also highest for TB-3	Z-scheme heterojunction	[33]
α–β phase Bi_2O_3 heterojunction	Rhodamine B (RhB), Methyl orange (MO)	Visible light (300 W Xe lamp)	98% RhB (60 min) and 96% MO (15 min)	α/β-phase homojunction (heterojunction between polymorphs	[35]
Bi/Bi_2O_3 -TiO_2	Methyl orange (MO), Rhodamine B (RhB),	500 W Xe lamp (CEL-S500), simulated solar irradiation	75% (PEC), 80% (PEC) in 180 min	Indirect (plasmon-mediated) Z-scheme *via* metallic Bi^0 as electron mediator/bridge	[56]
β-Bi_2O_3/Bi_2WO_6	Ciprofloxacin (CIP, antibiotic), 15 mg/L (100 mL)	300 W Xe lamp with cut-off filter, λ ≥ 400 nm (visible light)	~92-93% in 90 min	Z-scheme formed by band bending of a p-n junction:	[57]
Bi_2O_3/Bi_2WO_6	Indigo carmine (IC) dye, 50 mg/L (50 ppm)	UV-A lamp, λ = 365 nm (best of 4 sources tested: UV-A > Hg-lamp > UV-B ≈ LED	98.9% in 120 min	Type-II heterojunction	[60]
α-Bi_2O_3/Carbon Quantum Dots (C-dots)	Indigo carmine (IC) dye, simulated dye bath effluent and Levofloxacin (antibiotic)	85 W Oreva CFL bulb (visible light)	86% (120 min), 87% (180 min); 79% levofloxacin (120 min)	Electron-transfer/up-conversion mechanism	[130]
BiFeO3/Bi_2O_3 p–n heterojunction (auto-combustion synthesis)	Nitrobenzene (NB)	Solar irradiation and 15 W LED lamp (6500 K)	100% NB degradation under both solar (180 min) and LED (240 min)	p–n heterojunction/direct charge transfer	[137]
Nitrogen-doped α-Bi_2O_3- *g*-C_3N_4, heterojunction ($N_{0.1}$/Bi_2O_3-*g*-C_3N_4, solvo thermal)	Rhodamine B (RhB, oxidation) and Cr(VI) (reduction)	400 W Mercury vapour lamp (General Electric) with λ ≥ 420 nm cutoff (visible light)	100% RhB and 90% Cr(VI) (120 min)	Z-scheme/heterojunction with N-doping-induced defects	[138]

tively charged holes behind. This process generates electron–hole (e^-/h^+) pairs that initiate subsequent photocatalytic reactions. The excitation process can be represented as follows:

$$Bi_2O_3 + h\nu \rightarrow Bi_2O_3 (e_{CB}^- + h_{VB}^+) \quad (1)$$

Once generated, the photogenerated charge carriers diffuse to the catalyst surface and become involved in surface mediated oxidation and reduction reactions. Electrons accumulated in the conduction band reduce adsorbed oxygen molecules to form superoxide radicals ($^\bullet O_2^-$), whereas the valence band holes act as strong oxidizing species by reacting with water or surface hydroxyl groups. The formation of superoxide radicals is described by the following reaction:

$$e_{CB}^- + O_2 \rightarrow {}^\bullet O_2^- \quad (2)$$

The generated superoxide radicals may further react with protons and electrons to produce H_2O_2 and hydroxyl radicals through a series of intermediate reactions:

$$^\bullet O_2^- + H^+ \rightarrow {}^\bullet HO_2 \quad (3)$$

$$2 \cdot HO_2 \rightarrow H_2O_2 + O_2 \quad (4)$$

$$H_2O_2 + e^- \rightarrow {}^\bullet OH + OH^- \quad (5)$$

In parallel, the valence band holes function as powerful oxidizing agents, converting surface-bound water molecules or hydroxyl ions into hydroxyl radicals ($^\bullet$OH), which are among the most reactive species responsible for the photocatalytic degradation of pollutants. The corresponding reaction is given by:

$$h_{VB}^+ + H_2O \rightarrow {}^\bullet OH + H^+ \quad (6)$$

or

$$h_{VB}^+ + OH^- \rightarrow {}^\bullet OH \quad (7)$$

In some Bi_2O_3 based systems, singlet oxygen is also generated as an additional reactive oxygen species (ROS), depending on the reaction environment and catalyst composition [10]. The highly oxidative radicals ($^\bullet$OH, $^\bullet O_2^-$), singlet oxygen and photogenerated holes collectively attack adsorbed organic contaminants, which result in the successive oxidation and mineralization reactions:

$$\text{Organic pollutant} + \text{ROS}/h^+ \rightarrow \text{Intermediates} \rightarrow CO_2 + H_2O + \text{Mineral acids} \quad (8)$$

or more generally,

$$\text{Dye} + {}^\bullet OH/{}^\bullet O_2^-/h^+ \rightarrow CO_2 + H_2O + \text{Inorganic ions} \quad (9)$$

Photocatalytic performance depends on the ability of a semiconductor to generate electron–hole pairs, suppress their recombination, facilitate charge transport and promote interfacial redox reactions. Pristine Bi_2O_3 often exhibits rapid electron–hole recombination, which limits its photocatalytic efficiency [4]. Heterostructure engineering offers an effective approach to overcoming this limitation. Depending on the band-edge alignment of the coupled semiconductors, Bi_2O_3-based composites can form type-II, p–n, Z-scheme, S-scheme or Schottky heterojunctions. Each configuration provides a distinct interfacial charge-transfer pathway that influences redox activity and photocatalytic efficiency [7,139-142]. These architectures improve charge separation while preserving suitable oxidation and reduction potentials. Understanding the underlying charge-transfer mechanisms is essential for the rational design and optimization of high-performance Bi_2O_3-based photocatalysts.

Photocatalytic water splitting and H_2 generation: The photocatalytic water splitting is an attractive solar to chemical energy conversion process for the generation of H_2, which is considered a promising clean energy carrier for a sustainable energy future. In semiconductor photocatalysts, incident photons with energy equal to or higher than the band gap generate electron–hole pairs. The conduction-band (CB) electrons participate in the hydrogen evolution reaction (HER), while valence-band (VB) holes drive the oxygen evolution reaction (OER). The general water-splitting reaction is expressed as: $2H_2O \rightarrow 2H_2 + O_2$. The minimum thermodynamic energy requirement for water splitting is 1.23 eV, corresponding to the potential difference between the H^+/H_2 and O_2/H_2O redox couples. The practical photocatalytic systems require additional energy to overcome reaction overpotentials, particularly those associated with the kinetically sluggish OER [143,144]. An efficient photocatalyst should possess suitable band-edge positions, effective light absorption, efficient charge separation, transport and favourable surface reaction kinetics.

Hydrogen generation has received considerable attention in photocatalytic energy conversion owing to the potential of H_2 as a solar-derived chemical fuel. Many studies on Bi_2O_3-based photocatalysts evaluate performance primarily through the H_2 evolution rate rather than simultaneous stoichiometric production of H_2 and O_2. In such systems, photogenerated electrons reduce protons to H_2, while sacrificial electron donors may consume photogenerated holes and limit charge-carrier recombination. H_2 evolution under these conditions should be distinguished from the water splitting, which requires simultaneous generation of H_2 and O_2 through coupled reduction and oxidation reactions. This distinction is important when comparing the reported hydrogen production performance of Bi_2O_3-based materials.

Bi_2O_3 has attracted interest as a visible-light-responsive semiconductor for photocatalytic energy conversion owing to its relatively narrow band gap and tunable electronic properties. Its application in hydrogen generation is restricted by rapid electron–hole recombination and band-edge positions that may not provide sufficient redox potentials for efficient water splitting. Heterojunction engineering offers an effective approach to overcoming these limitations. The construction of p–n heterojunctions and S-scheme architectures can promote spatial charge separation while preserving the redox potentials required for surface reactions.

Gao *et al.* [135] developed a 2D TiO_2/Bi_2O_3 S-scheme heterojunction for environmental remediation and hydrogen production. The intimate contact between TiO_2 and Bi_2O_3 nanosheets provided a large interfacial area and shortened the migration distance of photogenerated carriers. X-ray photoelectron spectroscopy, electron paramagnetic resonance, in situ irradiated XPS and theoretical calculations supported the proposed S-scheme charge-transfer mechanism. Selective recombination of relatively weak charge carriers preserved highly reducing electrons and strongly oxidizing holes. The optimized TiO_2/Bi_2O_3 photocatalyst achieved an H_2 evolution rate of 12.08 mmol h^{-1} g^{-1}. Shafiq *et al.* [136] employed a p–n heterojunction strategy to improve the hydrogen evolution performance of $Bi_2O_3/BiVO_4$ composites. The optimized 3% $Bi_2O_3/BiVO_4$ sample achieved an H_2 evolution rate of 171.13 μmol h^{-1} g^{-1}, approximately 16 times higher than that of the pristine material. The enhanced activity was linked to heterojunction formation and favourable morphological characteristics along with increased surface area and extended visible-light absorption. This study highlights the potential of combining Bi_2O_3 with other bismuth-based semiconductors for solar-driven H_2 generation.

A Cu-free $Bi_2O_3/Al_2Bi_{24}O_{39}/Al_2Bi_{48}O_{75}$ nanowire photocathode exhibited a photocurrent density of -4.85 mA cm^{-2} at 0 V *versus* RHE. The photocathode possessed a band gap of 1.83 eV and suitable conduction-band positioning for H_2 evolution. It maintained a photocurrent density of approximately -2 mA cm^{-2} over 2 h and generated 696 μmol cm^{-2} of H_2 with 93% Faradaic efficiency [145]. A porous $ZnBi_{38}O_{60}/\gamma$-Bi_2O_3 photocathode prepared through spray pyrolysis achieved a photocurrent density of -1.55 mA cm^{-2} at 0 V *versus* RHE. It exhibited a band gap of 2.3 eV and a specific surface area of 744 m^2 g^{-1} [146]. During continuous operation, the photocathode maintained -0.4 mA cm^{-2} for 1800 s with 100% Faradaic efficiency.

Yuan *et al.* [147] developed a MOF-on-MOF-derived hollow ZnO/Bi_2O_3 heterostructure for photocatalytic H_2 generation. The composite achieved an H_2 evolution rate of 3243.2 μmol h^{-1} g^{-1}, approximately 16.2 times higher than pristine Bi_2O_3. The enhanced activity was attributed to its hollow architecture, abundant active sites, improved light absorption and efficient interfacial charge separation between ZnO and Bi_2O_3. Alkallas *et al.* [148] developed a mushroom-like Bi_2MoO_6-Bi_2O_3/poly(1*H*-pyrrole) core-shell nanocomposite photocathode for hydrogen generation using sanitation water as the electrolyte. The system achieved an H_2 evolution rate of 2.5 μmol h^{-1} cm^{-2} with a band gap of ~1.7-1.75 eV. The composite exhibited a photocurrent density of -0.45 mA cm^{-2} under full-spectrum white-light irradiation. Its enhanced performance was linked to broad visible-to-infrared light absorption, nanoscale crystallinity (~ 35 nm) and the synergistic interaction between the Bi_2MoO_6-Bi_2O_3 components and polymer matrix. This approach offers an opportunity to combine hydrogen generation with wastewater valorization.

Khalid *et al.* [149] developed a Bi_2O_3/MoS_2 p–n heterojunction photocatalyst. The composite containing 11 wt.% Bi_2O_3 achieved the highest H_2 evolution rate of 10 μmol h^{-1} g^{-1}, nearly ten times higher than those of pristine Bi_2O_3 and MoS_2. The improved activity was attributed to extended visible light absorption, increased surface area and efficient charge-carrier separation across the p–n interface. Nguyen & Edalati [150] synthesized defective and strained black Bi_2O_3 through high-pressure torsion. The resulting material exhibited a tenfold enhancement in photocatalytic H_2 production with good cycling stability. Oxygen vacancies and lattice strain modified the electronic structure and improved light absorption while suppressing electron–hole recombination. These structural changes contributed to enhanced hydrogen evolution activity.

Fu *et al.* [151] developed a direct Z-scheme Bi_2O_3/Bi_2MoO_6 heterojunction by growing Bi_2O_3 *in situ* on Bi_2MoO_6 under alkaline conditions using NaOH or KOH followed by calcination in air. The direct Z-scheme charge-transfer pathway facilitated charge separation while preserving suitable redox potentials. The composite achieved 96.4% phenol degra-

dation and an H_2 evolution rate of 52 μmol g^{-1} under visible light irradiation. Xie *et al*. [33] prepared 0D/2D TiO_2 nanoparticle/Bi_2O_3 nanosheet heterojunctions through a sol-gel method followed by sonication. The resulting TB-*x* (*x* = 1, 2, 3 and 4) composites were evaluated for tetracycline (TC) degradation and H_2 generation under visible light irradiation. The optimized TB-3 sample containing 15 wt.% Bi_2O_3 achieved an H_2 production yield of 99.39 μmol g^{-1} compared with 76.15 μmol g^{-1} for pristine TiO_2. It exhibited the highest TC degradation efficiency among the investigated samples.

The reported studies establish that hydrogen generation in Bi_2O_3-based systems depends on light absorption, charge separation, interfacial carrier migration and surface reaction kinetics. Intimate heterointerfaces can reduce bulk electron–hole recombination, while S-scheme and related charge transfer mechanisms preserve the energetic electrons required for H_2 evolution. Morphological modifications improve surface accessibility and shorten carrier transport pathways. Suitable cocatalysts and charge-transfer mediators can further facilitate proton reduction. Table-5 summarizes the H_2 production performance of Bi_2O_3-based photocatalysts under different experimental conditions.

Photocatalytic CO_2 reduction: The photocatalytic CO_2 reduction offers a promising route for converting greenhouse gas into sustainable fuels and value-added chemicals. Under light irradiation, semiconductor photocatalysts generate electron–hole pairs through photon absorption. The conduction band electrons drive CO_2 reduction, while photogenerated holes participate in oxidation reactions involving water or sacrificial agents. Depending on the reaction pathway, CO_2 can be converted into CO, formic acid, methanol, methane and higher hydrocarbons. These reactions involve multiple proton-coupled electron-transfer steps and are hindered by the high chemical stability of CO_2. Rapid charge recombination, weak CO_2 adsorption and activation, and competing H_2 evolution further restrict conversion efficiency and product selectivity.

Bi_2O_3 has attracted interest as a visible-light-responsive semiconductor for photocatalytic CO_2 reduction owing to its relatively narrow band gap and suitable electronic structure. Pristine Bi_2O_3 suffers from rapid charge-carrier recombination and inefficient utilization of photogenerated electrons. The stable CO_2 molecule also requires activation through surface intermediates such as $CO_2^{\bullet-}$ and $^{\bullet}COOH$ before subsequent reduction steps can occur. Researchers have explored phase engineering, heterojunction construction and defect modification to address these limitations. Oxygen vacancies can improve CO_2 adsorption and activation, while surface modification and the incorporation of metallic or semiconductor components can facilitate charge separation and interfacial transfer. These approaches aim to improve CO_2 conversion efficiency and regulate product selectivity [152]. Liu *et al*. [153] reported an early example of defect-assisted CO_2 photoreduction using $Bi_2Al_4O_9$/β-Bi_2O_3 heterojunctions containing oxygen vacancies. The composite was synthesized through a one-step *in situ* self-combustion method. The relative proportions of $Bi_2Al_4O_9$ and β-Bi_2O_3 were controlled by adjusting the $Bi(NO_3)_3$/$Al(NO_3)_3$ ratio. The photocurrent and surface photovoltage measurements confirmed improved charge

TABLE-5
PHOTOCATALYTIC HYDROGEN PRODUCTION RATE OF Bi_2O_3 BASED PHOTOCATALYSTS

Photocatalyst	Method	Reaction condition	Band gap (eV)	Light source	Hydrogen evolution (H_2 gas)	Ref.
0D/2D TiO_2/Bi_2O_3	Sol–gel method and followed by sonication	50 mg catalyst with10 mL methanol and 165 μL chloroplatin acid	2.3	300 W xenon lamp, Visible light irradiation.	99.39 μmol g^{-1}	[33]
2D/2D TiO_2/Bi_2O_3	Hydrothermal	10 vol% TEOA; water splitting	TiO_2=3.2 Bi_2O_3= 2.8	365 nm LED	12.08 mmol g^{-1} h^{-1}	[135]
$Bi_2O_3BiVO_4$	Hydrothermal	400 mL; 0.04 M Na_2SO_3 + 0.1 M Na_2S; catalyst 50 mg	Bi_2O_3=2.8 $BiVO_4$=2.4	Visible light, λ > 420 nm	171.13 μmol g^{-1} h^{-1}	[136]
$Bi_2O_3Al_2Bi_{24}O_{39}$/$Al_2Bi_{48}O_{75}$	Spray pyrolysis	Bi:Al = 21:1; 0 V_{rhe}; 2 h	1.83	Simulated sunlight	696 μmol cm^{-2} (2 h)	[145]
$ZnBi_{38}O_{60}$/ γ-Bi_2O_3	Spray pyrolysis	pH 6.99; 0 V *vs*. RHE; PEC water splitting	2.83	Illumination; 480 nm for IPCE	H_2 produced; 100% Faradaic efficiency	[146]
ZnO/Bi_2O_3	MOF-on-MOF derived; calcination	Photocatalytic water splitting with sacrificial agent	NA	Simulated sunlight	3243.2 μmol h^{-1} g^{-1}	[147]
Bi_2MoO_6–Bi_2O_3P1HP	Two-step synthesis: reflux preparation of Bi_2MoO_6–Bi_2O_3 followed by oxidative polymerization	Bi_2MoO_6-Bi_2O_3/P1HP C-S photocathode using sanitation water	1.75	White light monochromatic illumination 340–730 nm	2.5 μmol h^{-1} cm^{-2}; J_{ph} = –0.45 mA cm^{-2} under full-spectrum white light; –0.42 mA cm^{-2} at 340 nm	[148]
Bi_2O_3/MoS_2	Two-step hydrothermal synthesis; Bi_2O_3 loading varied from 0–15 wt.%	Water-splitting system	Bi_2O_3=2.8 eV MoS_2=1.29 eV	Visible-light irradiation	10 μmol h^{-1} g^{-1}	[149]
Defective Bi_2O_3	High-pressure torsion (HPT) of α-Bi_2O_3; 6 GPa, 1 rpm; N = 10 turns → oxygen vacancies + lattice strain	50 mg catalyst + 27 mL H_2O + 3 mL CH_3OH (sacrificial agent) + 0.25 mL 0.1 M $Pt(NH_3)_4(NO_3)_2$ (Pt co-catalyst); Ar purging; 180 min irradiation	2.6	300 W Xe lamp, full-arc spectrum; 18 kW m^{-2}	19.88 mmol m^{-2} h^{-1} (59.6 mmol m^{-2} after 3 h)	[150]
Bi_2O_3/Bi_2MoO_6	Alkali-assisted *in situ* growth of Bi_2O_3 on Bi_2MoO_6 followed by air calcination	20 mg catalyst; aqueous H_2-evolution reaction under visible-light irradiation.	Bi_2O_3=2.8 eV; Bi_2MoO_6= 2.4–2.8	300 W Xe lamp, visible light	52 μmol g^{-1}	[151]

separation, while CO_2 temperature-programmed desorption revealed enhanced CO_2 adsorption. The optimized composite containing 14 mol% $Bi_2Al_4O_9$ exhibited the highest CO_2-to-CO conversion activity. Its improved performance was attributed to the combined effects of heterojunction-mediated charge separation and oxygen vacancies that provided favourable sites for CO_2 adsorption and activation [153].

He *et al.* [154] developed a core shell Bi_2O_3/Bi_2WO_6@ *g*-C_3N_4 photocatalyst with Bi_2O_3/Bi_2WO_6 as the core and *g*-C_3N_4 as the shell. Strong interfacial interactions facilitated charge transfer and reduced charge-transfer resistance. The optimized composite achieved a CO production yield of 263.7 μmol g^{-1} with 97.0% selectivity. DRIFTS and density functional theory (DFT) calculations identified •COOH formation as the rate-determining step and established the importance of CO intermediate adsorption and desorption [154]. She *et al.* [155] synthesized Bi_2O_3 quantum dots on ultrathin $SrBi_4Ti_4O_{15}$ nanosheets through a hydrothermal method. The quantum dots provided additional active sites and shortened electron-transport distances. The optimized heterostructure achieved CO and CH_4 yields of 73.0 and 30.2 μmol g^{-1}, respectively. These values represented approximately threefold and 30-fold increases over pristine $SrBi_4Ti_4O_{15}$. DFT calculations and electron paramagnetic resonance measurements supported an S-scheme charge-transfer mechanism. *In situ* infrared spectroscopy identified bidentate formate species as key reaction intermediates [155].

Xu *et al.* [156] developed a $Bi_2O_3/Bi_2Sn_2O_7$ heterojunction through a one-step hydrothermal method for photocatalytic CO_2 reduction. The optimized composite achieved a CO production yield of 186.40 μmol g^{-1} and outperformed pristine $Bi_2Sn_2O_7$. Experimental measurements and DFT calculations supported an S-scheme charge-transfer mechanism involving electron transfer from Bi_2O_3 to $Bi_2Sn_2O_7$. This arrangement improved charge separation while retaining electrons with sufficient reducing power for CO_2 conversion. The catalyst maintained approximately 96.5% of its initial CO production after six cycles. Dai *et al.* [157] engineered a Bi nanocluster/α-Bi_2O_3 interface to modify the active sites for photocatalytic CO_2 reduction. Deposited Bi nanoclusters shifted the dominant surface-active sites towards metallic Bi and promoted electron transfer from α-Bi_2O_3 to the clusters. The modified interface improved CO_2 adsorption and activation and achieved 94.8% CH_4 selectivity with approximately 210-fold higher activity than pristine α-Bi_2O_3 based on transferred electrons. The mechanistic analysis indicated that •CO underwent further hydrogenation at Bi sites rather than desorbing as CO.

Tang *et al.* [158] developed a 0D/3D CD/Bi_2O_3 microflower heterostructure with an S-scheme charge transfer pathway. The porous Bi_2O_3 structure provided accessible surface sites for CO_2 adsorption, while interfacial charge transfer improved charge separation and preserved strongly reducing electrons. This work illustrates the role of porous morphology and heterointerface engineering in photocatalytic CO_2 conversion. Han *et al.* [159] developed an oxygen deficient Bi_2O_{3-x}/NiAl-LDH 2D/2D S-scheme heterojunction for photothermal-assisted CO_2 reduction. Oxygen vacancies enhanced light absorption and contributed to photothermal conversion, while the intimate interface facilitated charge transfer. The optimized 50-BO/NA-LDH catalyst achieved a CO production rate of 83.55 ± 2.76 μmol g^{-1} h^{-1}. This value was approximately nine and 27 times higher than those of Bi_2O_{3-x} and NiAl-LDH, respectively [159]. Amari *et al.* [160] reported a ternary $Fe_2O_3/Bi_2O_3/g$-C_3N_4 S-scheme photo-catalyst for visible-light-driven CO_2 reduction. The multi-component architecture was designed to facilitate interfacial charge transfer while preserving the redox potential of photogenerated carriers. Their work further explored the potential of Bi_2O_3-based S-scheme systems for CO_2 conversion and environmental remediation.

Ojha & Pant [161] reported an α-Bi_2O_3/MIL-88A heterostructure formed by coupling α-Bi_2O_3 nanospheres with spindle shaped Fe-based MIL-88A through electrostatic interactions. The composite exhibited a band gap of ~1.75 eV and facilitated CO_2 conversion into CO, CH_4 and H_2 in water without sacrificial agents or noble-metal cocatalysts. Wang *et al.* [152] developed an α/β-Bi_2O_3 heterophase junction through a rapid 5 minutes microwave-assisted synthesis. The resulting material contained nitrogen derived from the nitrate precursor. The combination of nitrogen doping, hetero-phase junction formation and porous morphology improved visible-light absorption and charge separation. The optimized photocatalyst achieved a CO_2 reduction rate of 35.18 μmol g^{-1} h^{-1}. This value was 1.10 and 5.83 times higher than those of α-Bi_2O_3 and β-Bi_2O_3, respectively.

Guo *et al.* [162] developed a metallic Bi/Bi_2O_3 Ohmic junction by introducing Bi onto Bi_2O_3 nanosheets. The interface facilitated directional charge transfer and suppressed charge-carrier recombination, while localized surface plasmon resonance improved light absorption and photothermal conversion. The optimized photocatalyst achieved a methanol production rate of 610 μmol g^{-1} under light irradiation. The experimental and theoretical investigations revealed that interfacial Bi sites promoted CO_2 activation towards •COOH, while metallic Bi sites facilitated subsequent protonation steps. Zhang *et al.* [163] developed an oxygen vacancy rich BiOCl/Bi_2O_3 Z-scheme heterojunction using Bi_2O_3 derived from the bismuth-based MOF CAU-17. The composite consisted of BiOCl nanoplates and hollow Bi_2O_3 rods with abundant accessible surface sites. Oxygen vacancies enhanced CO_2 adsorption and activation, while the Z-scheme architecture facilitated charge separation. Without a cocatalyst, the optimized photocatalyst achieved a CO production rate of 107.8 μmol g^{-1} h^{-1} under 300 W Xe lamp irradiation. A recent study [164] employed amorphous Bi_2O_3 in a Pd_1/Bi_1-décorated TiO_2 system for the conversion of CO_2 into multicarbon products. Amorphous Bi_2O_3 improved local CO_2 availability and facilitated charge transfer, while adjacent Pd and Bi sites promoted C–C coupling. The optimized catalyst achieved an ethane production rate of 212.5 μmol g^{-1} h^{-1} with ~90% selectivity and good durability without sacrificial agents. The mechanistic investigations indicated that CH_3-related intermediates formed on Pd sites participated in subsequent coupling near Bi sites. This approach illustrates the role of Bi_2O_3 in regulating the local reaction environment for multicarbon product formation.

The reported studies establish that the CO_2 photoreduction over Bi_2O_3-based materials depends on light absorption, charge separation, CO_2 activation and product selectivity. S-scheme and Z-scheme heterojunctions facilitate charge separation while retaining electrons with sufficient reduction potential. Oxygen vacancies and metallic Bi sites improve CO_2 adsorption and surface activation. The morphological modifications such as quantum dots, porous structures and nanosheets increase accessible active sites and shorten charge transport distances. Despite these advances, practical applications remain restricted by the high stability of CO_2, charge carrier recombination, competing H_2 evolution, limited product yields and poor selectivity towards multicarbon products.

Future scope: Further development of Bi_2O_3-based photocatalysts requires higher attention to the factors governing their performance under practical operating conditions. Future research should address the controlled modification of crystal structure, phase composition, morphology, defect states, oxygen vacancies, dopant chemistry and heterostructure interfaces to improve light absorption, charge-carrier separation and surface redox activity. Combining Bi_2O_3 with emerging materials such as MXenes, graphene derivatives, metal-organic frameworks (MOFs) and two-dimensional semiconductors, offers scope for developing multifunctional photocatalysts with improved interfacial charge transport and catalytic performance. A deeper understanding of photocatalytic pathways through *in situ*/operando characterization and theoretical modelling is equally important for establishing reliable structure property-performance relationships.

The practical relevance of Bi_2O_3-based photocatalysts needs to be assessed using complex wastewater systems containing mixtures of organic pollutants, pharmaceutical residues, antibiotics and heavy metals, rather than relying mainly on individual model dyes. Their application in CO_2 reduction and water splitting deserves better attention, particularly in relation to product selectivity, conversion efficiency, charge-carrier utilization and solar-to-hydrogen conversion efficiency. Appropriate band-edge engineering, modification of surface active sites and incorporation of suitable cocatalysts could improve CO_2 conversion into value-added chemicals and fuels, along with photocatalytic hydrogen generation. Standardized testing procedures and extended stability studies under realistic reaction conditions are necessary to establish meaningful comparisons between different photocatalytic systems. Particular attention should also be given to catalyst recyclability, resistance to photocorrosion, long-term structural stability and the development of scalable, environmentally friendly and cost-effective synthesis routes. Moving beyond laboratory-scale experiments towards pilot-scale continuous-flow systems will be an important step in assessing the practical applicability of Bi_2O_3-based materials for wastewater treatment, solar-driven CO_2 conversion, water splitting and sustainable hydrogen production.

Conclusions

Bismuth oxide (Bi_2O_3) has attracted considerable attention as a visible-light-responsive semiconductor photocatalyst owing to its suitable band gap, broad visible-light absorption, favourable electronic structure, low toxicity and relatively simple, cost-effective synthesis. This review has examined the crystal structures, synthesis methods and physico-chemical properties of Bi_2O_3, with particular emphasis on the photocatalytic behaviour of pristine, doped and heterostructured materials. Although pristine Bi_2O_3 exhibits promising photocatalytic activity under visible light, rapid electron-hole recombination, which limited surface-active sites and photocorrosion restrict its performance. Elemental doping, defect engineering, morphology control and heterojunction formation provide effective routes for modifying its electronic structure, improving light absorption, promoting charge separation and enhancing photocatalytic stability. The reported studies establish the potential of Bi_2O_3-based photocatalysts for degrading various organic pollutants such as dyes, antibiotics, pharmaceutical residues and other emerging contaminants. Their antimicrobial properties further extend their relevance to environmental applications. The potential of Bi_2O_3-based nanostructures extends beyond pollutant degradation to photocatalytic CO_2 reduction, water splitting and hydrogen generation. Their performance in these reactions depends on the suitable band-edge positions, interfacial charge transfer, carrier transport, surface reaction kinetics and the selection of appropriate cocatalysts. Heterostructure engineering has received particular attention as a means of controlling charge-carrier migration and limiting electron–hole recombination. A clear understanding of reactive species, such as $^{\bullet}OH$, $^{\bullet}O_2^-$ and h^+, along with the charge-transfer pathways proposed in type-II, Z-scheme and S-scheme heterojunctions, is essential for establishing reliable photocatalytic mechanisms and guiding material design. The transition of Bi_2O_3-based photocatalysts from laboratory investigations to practical applications requires further research into scalable synthesis, structural stability, recyclability and performance under realistic operating conditions. The mechanistic studies supported by experimental characterization and theoretical calculations are needed to establish the relationship between material properties and photocatalytic activity. More attention should be given to product selectivity and conversion efficiency during CO_2 reduction as well as solar-to-hydrogen conversion during water splitting. The development of durable, cost-effective and environmentally sustainable photocatalytic systems, supported by long-term testing and pilot-scale validation, will be important for establishing the practical relevance of Bi_2O_3-based materials in environmental remediation and solar energy conversion.

CONFLICT OF INTEREST

The authors declare that there is no conflicts of interest regarding the publication of this article.

DECLARATION OF AI-ASSISTED TECHNOLOGIES

During the preparation of this manuscript, the authors used an AI-assisted tool(s) to improve the language and no data, results or scientific conclusions were generated by AI. All analyses, interpretations and conclusions are the authors' own. The authors reviewed and edited the content and take full responsibility for the published work.

REFERENCES

1. L. Chen, B. Guan, J. Guo, Y. Chen, Z. Ma, J. Chen, S. Yao, C. Zhu, H. Dang, K. Shu, Z. Guo, C. Yi, K. Shi, Y. Li, J. Hu and Z. Huang, *Catal. Sci. Technol.*, **13**, 5478 (2023); https://doi.org/10.1039/D3CY00760J
2. O.A. Putra, D.N.I. Saputra and F.B. Arafat, *Radiat. Eff. Defects Solids*, **181**, 1288 (2025); https://doi.org/10.1080/10420150.2025.2592201
3. V. Mane, D. Dake, N. Raskar, R. Sonpir, E. Stathatos and B. Dole, *Chem. Phys. Impact*, **8**, 100517 (2024); https://doi.org/10.1016/j.chphi.2024.100517
4. A.L. Ruiz-Castillo, M. Hinojosa-Reyes, R. Camposeco and L. Hinojosa-Reyes, *Inorg. Chem. Commun.*, **183**, 115730 (2026); https://doi.org/10.1016/j.inoche.2025.115730
5. D. Dash, N.R. Panda and D. Sahu, *Appl. Surf. Sci.*, **494**, 666 (2019); https://doi.org/10.1016/j.apsusc.2019.07.089
6. R.R.S. Coronado-Castañeda, M.L. Maya-Treviño, E. Garza-González, J. Peral, M. Villanueva-Rodríguez and A. Hernández-Ramírez, *Catal. Today*, **341**, 82 (2020); https://doi.org/10.1016/j.cattod.2019.01.028
7. R. Shah, M. Chaudhary, M. Chauchan, A. Kumar, B. Pant and Mohit, *Asian J. Chem.*, **38**, 1663 (2026); https://doi.org/10.14233/ajchem.2026.36050
8. M. Bilal, M. Adeel, T. Rasheed, Y. Zhao and H.M. Iqbal, *Environ. Int.*, **124**, 336 (2019); https://doi.org/10.1016/j.envint.2019.01.011
9. G.W.A. Nyakairu, P.M. Kapanga, M. Ntale, S.N. Lusamba, R.M. Tshimanga, A. Ammari and Z. Shehu, *Clean. Water*, **1**, 100004 (2024); https://doi.org/10.1016/j.clwat.2024.100004
10. A.H. Zahid and Q. Han, *Nanoscale*, **13**, 17687 (2021); https://doi.org/10.1039/D1NR03187B
11. S. Bera, S. Ghosh and R.N. Basu, *New J. Chem.*, **42**, 541 (2018); https://doi.org/10.1039/C7NJ03424E
12. H. Najafian, F. Manteghi, F. Beshkar and M. Salavati-Niasari, *Separ. Purif. Tech.*, **209**, 6 (2019); https://doi.org/10.1016/j.seppur.2018.07.010
13. C. Manoharan, R. Rammohan, R. Subramanian and V. Umashanker, *Inorg. Nano-Met.*, **53**, 113 (2023); https://doi.org/10.1080/24701556.2021.1986526
14. P. Chen, H. Liu, W. Cui, S.C. Lee, L.A. Wang and F. Dong, *EcoMat*, **2**, e12047 (2020); https://doi.org/10.1002/eom2.12047
15. R. Li, W. Chen, H. Kobayashi and C. Ma, *Green Chem.*, **12**, 212 (2010); https://doi.org/10.1039/b917233e
16. P. Malathy, K. Vignesh, M. Rajarajan and A. Suganthi, *Ceram. Int.*, **40**, 101 (2014); https://doi.org/10.1016/j.ceramint.2013.05.109
17. L. Li, K. Zheng, Z. Li and Z. Chen, *J. Mater. Sci. Technol.*, **245**, 309 (2026); https://doi.org/10.1016/j.jmst.2025.04.026
18. Q. Han, L. Wang, J. Li, Y. Dong, Y. Ma, J. Zhang and S. Yu, *Chem. Eng. J.*, **519**, 165290 (2025); https://doi.org/10.1016/j.cej.2025.165290
19. H. Du, A. Zhang, Q. Zhang, Y. Sun, H. Zhu, H. Wang, Z. Tan, X. Zhang, X. Chen and G. Chen, *Separ. Purif. Tech.*, **359**, 130597 (2025); https://doi.org/10.1016/j.seppur.2024.130597
20. K. Cao, X. Ge, S. Li, Z. Tian, S. Cui, G. Guo, L. Yang, X. Li, Y. Wang, S. Bai, Q. Wei and W. Li, *RSC Adv.*, **15**, 17089 (2025); https://doi.org/10.1039/D5RA02399H
21. V. Ruiz-Santoyo, S. García-Carvajal and M.C. Arenas-Arrocena, *J. Nanopart. Res.*, **27**, 23 (2025); https://doi.org/10.1007/s11051-024-06207-9
22. A. Meher, A. Palai, N.R. Panda, S.P. Pati and D. Sahu, *Environ. Sci. Pollut. Res. Int.*, **32**, 22121 (2025); https://doi.org/10.1007/s11356-024-35804-3
23. F. Yu, C. Liu and S. Sharmin, *Proc. Assoc. Inf. Sci. Technol.*, **59**, 843 (2022); https://doi.org/10.1002/pra2.745
24. D. Leng, T. Wang, C. Du, X. Pei, Y. Wan and J. Wang, *Ceram. Int.*, **48**, 18270 (2022); https://doi.org/10.1016/j.ceramint.2022.03.085
25. A. Sharma, S. Kaur, R.K. Sharma and D. Sud, *Appl. Phys., A Mater. Sci. Process.*, **132**, 75 (2026); https://doi.org/10.1007/s00339-025-09269-1
26. D. Janardhana, S.N. Jayaramu, H.R. Anthony and H.C. Swart, *Mater. Sci. Semicond. Process.*, **192**, 109455 (2025); https://doi.org/10.1016/j.mssp.2025.109455
27. T. Saito, R. Ahmad, F. Kishimoto, T. Higashi, M. Katayama, L. Cavallo and K. Takanabe, *J. Mater. Chem. C Mater. Opt. Electron. Devices*, **10**, 17925 (2022); https://doi.org/10.1039/D2TC03718A
28. J.Z. Hassan, Y. Zhang, A. Raza and G. Li, Bismuth-Based Materials for Environmental Remediation, 3–31 (2022).
29. F. Dong, T. Xiong, Y. Sun, Z. Zhao, Y. Zhou, X. Feng and Z. Wu, *Chem. Commun. (Camb.)*, **50**, 10386 (2014); https://doi.org/10.1039/C4CC02724H
30. Y. Sun, Z. Zhao, W. Zhang, C. Gao, Y. Zhang and F. Dong, *J. Colloid Interface Sci.*, **485**, 1 (2017); https://doi.org/10.1016/j.jcis.2016.09.018
31. F. Wang, K. Cao, Q. Zhang, X. Gong and Y. Zhou, *J. Mol. Model.*, **20**, 2506 (2014); https://doi.org/10.1007/s00894-014-2506-z
32. G. Fan, Z. Ma, X. Li and L. Deng, *Ceram. Int.*, **47**, 5758 (2021); https://doi.org/10.1016/j.ceramint.2020.10.162
33. L. Xie, P. Wu, Q. Lei, C. Xu, W. Huang, X. Chen, W. Huang, X. Chen, K. Yang and H. He, *Catalysts*, **13**, 583 (2023); https://doi.org/10.3390/catal13030583
34. A.A. Oladipo and F.S. Mustafa, *Beilstein J. Nanotechnol.*, **14**, 291 (2023); https://doi.org/10.3762/bjnano.14.26
35. J. Hou, C. Yang, Z. Wang, W. Zhou, S. Jiao and H. Zhu, *Appl. Catal. B*, **142-143**, 504 (2013); https://doi.org/10.1016/j.apcatb.2013.05.050
36. J. Divya, N.J. Shivaramu, E. Coetsee, R.E. Kroon, W. Purcell and H.C. Swart, *J. Alloys Compd.*, **842**, 155641 (2020); https://doi.org/10.1016/j.jallcom.2020.155641
37. T.L. Wakjira, A.B. Gemta, G.B. Kassahun, D.M. Andoshe and K. Tadele, *ACS Omega*, **9**, 8709 (2024); https://doi.org/10.1021/acsomega.3c08939
38. F. Fahim, M. Ramzan, M.W. Mukhtar, Z. Nazeer, M.N. Akhtar, K.M. Katubi, M.S. Al-Buriahi and S. Ullah, *J. Mol. Graph. Model.*, **137**, 109019 (2025); https://doi.org/10.1016/j.jmgm.2025.109019
39. A. Meher, N.R. Panda, S. Jal and D. Sahu, *Surf. Interfaces*, **72**, 107225 (2025); https://doi.org/10.1016/j.surfin.2025.107225
40. A. Nyabadza, É. McCarthy, M. Makhesana, S. Heidarinassab, A. Plouze, M. Vazquez and D. Brabazon, *Adv. Colloid Interface Sci.*, **321**, 103010 (2023); https://doi.org/10.1016/j.cis.2023.103010
41. A.V. Nikam, B.L.V. Prasad and A.A. Kulkarni, *CrystEngComm*, **20**, 5091 (2018); https://doi.org/10.1039/C8CE00487K
42. S. Esposito, *Materials*, **12**, 668 (2019); https://doi.org/10.3390/ma12040668
43. Y. Astuti, B.M. Listyani, L. Suyati and A. Darmawan, *Indones. J. Chem.*, **21**, 108 (2020); https://doi.org/10.22146/ijc.53144
44. S.D. Khairnar and V.S. Shrivastava, *SN Appl. Sci.*, **1**, 762 (2019); https://doi.org/10.1007/s42452-019-0761-4
45. H.A. Kashmery and S.I. El-Hout, *Opt. Mater.*, **135**, 113231 (2023); https://doi.org/10.1016/j.optmat.2022.113231
46. W. Matysiak, *Sci. Rep.*, **12**, 4046 (2022); https://doi.org/10.1038/s41598-022-07830-z
47. Y. Astuti, A. Muslim and A. Darmawan, *Bull. Chem. React. Eng. Catal.*, **21**, 11 (2026); https://doi.org/10.9767/bcrec.20452
48. D. Akşit, C. Sayil and G.S.P. Soylu, *J. Sol-Gel Sci. Technol.*, **113**, 868 (2025); https://doi.org/10.1007/s10971-025-06668-x
49. A.U.R. Khan, M. Ramzan, S.J.F. Alanazi, A.M. Al-Mohaimeed, S. Ali, M. Imran, M.A. Majid and M.H. Sarfraz, *ACS Omega*, **9**, 22650 (2024); https://doi.org/10.1021/acsomega.3c10521

50. S. Essenni, F. Baragh, R. El Kaim Billah, I. Khaddoudi, L. Bahsis and M. Agunaou, *J. Inorg. Organomet. Polym. Mater.*, **35**, 1997 (2025); https://doi.org/10.1007/s10904-024-03410-y
51. J. Divya, N.J. Shivaramu, W. Purcell, W.D. Roos and H.C. Swart, *Appl. Surf. Sci.*, **520**, 146294 (2020); https://doi.org/10.1016/j.apsusc.2020.146294
52. C.R. Michel, *Sens. Technol.*, **2**, 2416649 (2024); https://doi.org/10.1080/28361466.2024.2416649
53. A. Urooj, M. Rani, A.A. Shah, S. Aslam, R. Siddiqui, A. Siddiqa, R. Neffati and A.D. Chandio, *RSC Adv.*, **12**, 32986 (2022); https://doi.org/10.1039/D2RA04760H
54. Sh. Labib, *J. Saudi Chem. Soc.*, **21**, 664 (2017); https://doi.org/10.1016/j.jscs.2015.11.003
55. S. Patil and S. Jagadale, eds.: R. Mane, V. Jadhav and A. Al-Enizi, Co-Precipitation Methods for the Synthesis of Metal Oxide Nanostructures, In: Solution Methods for Metal Oxide Nanostructures, Elsevier, pp. 39-60 (2023); https://doi.org/10.1016/B978-0-12-824353-4.00016-6
56. Z. Liu, Q. Wang, X. Tan, S. Zheng, H. Zhang, Y. Wang and S. Gao, *J. Alloys Compd.*, **815**, 152478 (2020); https://doi.org/10.1016/j.jallcom.2019.152478
57. C.X. Li, S.Y. Song, D.S. Shi, Y. Ying, X.X. Zhang, J.Q. Wei, B. Hong, J.C. Xu, H.X. Jin, P.F. Wang and X.Q. Wang, *J. Nanopart. Res.*, **22**, 123 (2020); https://doi.org/10.1007/s11051-020-04873-z
58. Y. Peng, M. Yan, Q.-G. Chen, C.-M. Fan, H.-Y. Zhou and A.-W. Xu, *J. Mater. Chem. A Mater. Energy Sustain.*, **2**, 8517 (2014); https://doi.org/10.1039/C4TA00274A
59. T. Li, X. Chang, L. Mei, X. Shu, J. Ma, L. Ouyang and S. Gu, *Nanoscale Adv.*, **3**, 5312 (2021); https://doi.org/10.1039/D1NA00443C
60. M.A. Sayed, S.M.A. El-Gamal, M. Ramadan, F.M. Helmy and A. Mohsen, *Sci. Rep.*, **15**, 17260 (2025); https://doi.org/10.1038/s41598-025-01925-z
61. C.V. Maestre and G.N. Santos, *Sci. Rep.*, **13**, 1787 (2023); https://doi.org/10.1038/s41598-023-27623-2
62. C. Li, Y. Ma, S. Zheng, C. Hu, F. Qin, L. Wei, C. Zhang, S. Duo and Q. Hu, *J. Colloid Interface Sci.*, **576**, 291 (2020); https://doi.org/10.1016/j.jcis.2020.02.115
63. A.S. Mandawade, L.D. Sonawane, H.I. Ahemad, Y.B. Aher, A.B. Gite, L.K. Nikam, G.H. Jain, M.D. Femi, G.E. Patil, B.M. Palve and M.S. Shinde, *J. Mater. Sci. Mater. Electron.*, **35**, 989 (2024); https://doi.org/10.1007/s10854-024-12739-6
64. G. Raja, A. Elumalai, P. Uma, V. Selvarani and K. Sudhakar, *Chem. Afr.*, **8**, 5823 (2025); https://doi.org/10.1007/s42250-025-01488-6
65. S. Sood, A. Umar, S.K. Mehta and S.K. Kansal, *Ceram. Int.*, **41(3A)**, 3355 (2015); https://doi.org/10.1016/j.ceramint.2014.10.038
66. M. Bagheri, M. Heydari and M.R. Vaezi, *J. Phys. Chem. Solids*, **112**, 14 (2018); https://doi.org/10.1016/j.jpcs.2017.08.020
67. S. Ansari, M.S. Ansari, S.P. Satsangee and R. Jain, *J. Pharm. Anal.*, **11**, 57 (2021); https://doi.org/10.1016/j.jpha.2020.03.013
68. K.B. Kusuma, M. Manju, C.R. Ravikumar, V.G. Dileepkumar, A.N. Kumar, M. Santosh, H.C.A. Murthy and K. Gurushantha, *J. Nanomater.*, **2022**, 3256611 (2022); https://doi.org/10.1155/2022/3256611
69. G.K. Dinesh and R. Saranya, *Water Air Soil Pollut.*, **235**, 621 (2024); https://doi.org/10.1007/s11270-024-07355-3
70. N.R. Panda, B.S. Acharya, P. Nayak and B.P. Bag, *Ultrason. Sonochem.*, **21**, 582 (2014); https://doi.org/10.1016/j.ultsonch.2013.08.007
71. A.O. Flayyih, W.K. Mahdi, Y.I.M. Abu Zaid and F.H. Musa, *Chem. Methodol.*, **6**, 620 (2022); https://doi.org/10.22034/chemm.2022.342124.1522
72. M.W. Alam, N. Allag, M. Utami, M. Waheed-Ur-Rehman, M. Al Saleh Al-Othoum and S. Sadaf, *J. Compos. Sci.*, **8**, 47 (2024); https://doi.org/10.3390/jcs8020047
73. P.L. Meena, A.K. Surela and L.K. Chhachhia, *Mater. Res. Innov.*, **28**, 236 (2024); https://doi.org/10.1080/14328917.2023.2258469
74. P. Moorthy and H.P. Kavitha, *ACS Omega*, **8**, 14752 (2023); https://doi.org/10.1021/acsomega.3c00792
75. K.C. Sunil Kumar, S. Chandra, V. Lakshmi Ranganatha, G.S. Shivaganga and C. Mallikarjunaswamy, *Nano-Struct. Nano-Objects*, **38**, 101159 (2024); https://doi.org/10.1016/j.nanoso.2024.101159
76. V. Lakshmi Ranganatha, G.S. Shivaganga, S. Pramila, G. Nagaraju, P. Parameswara, A.-B. Al-Odayni, C. Mallikarjunaswamy and A.A. Al-Kahtani, *Ionics*, **31**, 3537 (2025); https://doi.org/10.1007/s11581-025-06109-3
77. M.A. Hamada, O.M. Sadek, W.K. Mekhamer, I.H. Saleh and M. Elsafi, *Sci. Rep.*, **15**, 40352 (2025); https://doi.org/10.1038/s41598-025-26415-0
78. S. Ali, M. Imran, R. Kousar, M. Fatima, M.Z. Manzoor, H.E. Ahmed, S. Riaz, H. Ullah, A. Nazir and Z. Batool, *Desalination Water Treat.*, **320**, 100688 (2024); https://doi.org/10.1016/j.dwt.2024.100688
79. A. Negash, L.M. Derseh, A. Tedla and J.M. Yassin, *Sci. Rep.*, **14**, 23393 (2024); https://doi.org/10.1038/s41598-024-74408-2
80. T.L. Soundarya, M. Divya, R.T. Nayana, G. Nagaraju, B. Nirmala and R. Harini, *Inorg. Chem. Commun.*, **185**, 116038 (2026); https://doi.org/10.1016/j.inoche.2025.116038
81. A. Kumar, Y. Kuang, Z. Liang and X. Sun, *Mater. Today Nano*, **11**, 100076 (2020); https://doi.org/10.1016/j.mtnano.2020.100076
82. V.N. Sonkusare, R.G. Chaudhary, G.S. Bhusari, A.R. Rai and H.D. Juneja, *Nano-Struct. Nano-Objects*, **13**, 121 (2018); https://doi.org/10.1016/j.nanoso.2018.01.002
83. M. Yahyazadehfar, E. Sheikhhosseini, S.A. Ahmadi and D. Ghazanfari, *Front Chem.*, **10**, 951229 (2022); https://doi.org/10.3389/fchem.2022.951229
84. V.Q. Nguyen, M.A. Mahadadalkar, A.M. Rabie and J.-J. Shim, *Environ. Sci. Nano*, **9**, 1724 (2022); https://doi.org/10.1039/D1EN01166A
85. M.Y.A. Mohamed, H. Ferjani, O.A. Oyewo, O.E. Ogunjinmi, S.M. Hamed, C. Amairia, S. Makgato and D.C. Onwudiwe, *Inorg. Chem. Commun.*, **165**, 112557 (2024); https://doi.org/10.1016/j.inoche.2024.112557
86. V.Q. Nguyen, M.A. Mahadadalkar, P.C. Nam, J.-J. Shim, J. Singh, B. Van and D.D. Nguyen, *J. Taiwan Inst. Chem. Eng.*, **166**, 105520 (2025); https://doi.org/10.1016/j.jtice.2024.105520
87. L. Hu, G. Zhang, M. Liu, Q. Wang and P. Wang, *Environ. Sci. Pollut. Res. Int.*, **25**, 4656 (2018); https://doi.org/10.1007/s11356-017-0871-8
88. Y. Zhang, Q. Shao, C. Chen, H. Jiang, F. Su, Q. Hu and Z. Guo, *Powder Technol.*, **370**, 226 (2020); https://doi.org/10.1016/j.powtec.2020.05.068
89. M.K. Hossain, G.F. Samu, K. Gandha, S. Santhanagopalan, J.P. Liu, C. Janáky and K. Rajeshwar, *J. Phys. Chem. C Nanomater. Interfaces*, **121**, 8252 (2017); https://doi.org/10.1021/acs.jpcc.6b13093
90. A. Bashir, S.S. Mestry, P. Vashishtha, G. Gupta and G.A. Bhaduri, *Luminescence*, **38**, 568 (2023); https://doi.org/10.1002/bio.4484
91. R.N. Keshava Murthy, M. Shivanna, N. Nasir Ahamed, V. Bhoomika, C.R. Ravikumar and H.C. Ananda Murthy, *Mater. Sci. Eng. B*, **307**, 117487 (2024); https://doi.org/10.1016/j.mseb.2024.117487
92. T.A. Gadhi, A. Hernández-Gordillo, M. Bizarro, P. Jagdale, A. Tagliaferro and S.E. Rodil, *Ceram. Int.*, **42**, 13065 (2016); https://doi.org/10.1016/j.ceramint.2016.05.087
93. S. Tabassum, M. Sahadat Hossain, D. Islam and S. Ahmed, *Surf. Interfaces*, **18**, 100371 (2025); https://doi.org/10.1016/j.rsurfi.2024.100371
94. Z. Liang, Y. Cao, Y. Li, J. Xie, N. Guo and D. Jia, *Appl. Surf. Sci.*, **390**, 78 (2016); https://doi.org/10.1016/j.apsusc.2016.08.085
95. L. Li, J. Jiang, X. Luan, C. Feng, Q. Yang, M. Chen and M. Zhang, *J. Optoelectron. Adv. Mater.*, **17**, 372 (2015).
96. Y. Peng, K.K. Wang, T. Liu, J. Xu and B.G. Xu, *Appl. Catal. B*, **203**, 946 (2017); https://doi.org/10.1016/j.apcatb.2016.11.011

97. Y. Ma, Q. Han, T.-W. Chiu, X. Wang and J. Zhu, *Catal. Today*, **340**, 40 (2020); https://doi.org/10.1016/j.cattod.2018.10.005
98. E.V. Timakova, T.E. Timakova and L.I. Afonina, *Chim. Techno Acta*, **10**, 202310304 (2023); https://doi.org/10.15826/chimtech.2023.10.3.04
99. W. Li, Q. Tian, X. Wang, Y. Qiu, B. Liu, W. Ma, Z. Liu, Q. Ren, H. Zhang, J. Yan, J. Yun, Z. Zhang, W. Zhao and Y. Wang, *Sens. Actuators B Chem.*, **438**, 137812 (2025); https://doi.org/10.1016/j.snb.2025.137812
100. R.I. Kamel, D.S. Ahmed and U.M. Nayef, *Optik*, **193**, 163013 (2019); https://doi.org/10.1016/j.ijleo.2019.163013
101. M. Alheshibri, S.A. Haladu, I. Al-Naib, Q.A. Drmosh, E. Çevik and K.A. Elsayed, *Arab. J. Chem.*, **19**, 2772025 (2025); https://doi.org/10.25259/AJC_277_2025
102. S. Elashmawi and A.A. Menazea, *RSC Adv.*, **15**, 48325 (2025); https://doi.org/10.1039/D5RA08147E
103. S.S. Shaker, R.A. Ismail and D.S. Ahmed, *Silicon*, **14**, 107 (2022); https://doi.org/10.1007/s12633-020-00789-4
104. G.D. Lim, J.H. Yoo, M. Ji and Y.I. Lee, *J. Alloys Compd.*, **806**, 1060 (2019); https://doi.org/10.1016/j.jallcom.2019.07.319
105. F. Yang, X. Yu, Z. Liu, J. Niu, T. Zhang, J. Nie, N. Zhao, J. Li and B. Yao, *Mater. Today Commun.*, **26**, 101735 (2021); https://doi.org/10.1016/j.mtcomm.2020.101735
106. N.Z. Noor Azman, W.F.I. Wan Mohamed and R.M. Ramli, *Radiat. Phys. Chem.*, **195**, 110102 (2022); https://doi.org/10.1016/j.radphyschem.2022.110102
107. S. Liu, J. Zhang, Y. Tian, J. Sun, P. Huang, J. Li and G. Han, *Materials*, **16**, 4673 (2023); https://doi.org/10.3390/ma16134673
108. S. Wu, J. Fang, X. Xu, Z. Liu, X. Zhu and W. Xu, *Photochem. Photobiol.*, **88**, 1205 (2012); https://doi.org/10.1111/j.1751-1097.2012.01164.x
109. T.P. Gujar, V.R. Shinde and C.D. Lokhande, *Mater. Res. Bull.*, **41**, 1558 (2006); https://doi.org/10.1016/j.materresbull.2006.01.024
110. C.H. Jadhav, P.K. Pagare, K.K. Inamdar and L.D. Kadam, *Macromol. Symp.*, **387**, 1800198 (2019); https://doi.org/10.1002/masy.201800198
111. J. Sydorenko, M. Krunks, A. Katerski, R. Grzibovskis, A. Vembris, A. Mere, N. Spalatu and I.O. Acik, *RSC Adv.*, **14**, 19648 (2024); https://doi.org/10.1039/D4RA02907K
112. T. Takeyama, N. Takahashi, T. Nakamura and S. Itoh, *Solid State Commun.*, **133**, 771 (2005); https://doi.org/10.1016/j.ssc.2005.01.012
113. Z. Sun, D. Oka and T. Fukumura, *Cryst. Growth Des.*, **19**, 7170 (2019); https://doi.org/10.1021/acs.cgd.9b01033
114. A. Chauhan, R. Verma, J. Dhatwalia, A. Kumari, G. Chandrasekaran, V. Dutta, S. Ghotekar, M. Kaur, J. Vignesh and S. Thakur, *Biomass Convers. Biorefin.*, **14**, 25103 (2024); https://doi.org/10.1007/s13399-023-04679-8
115. P. Riente, M. Fianchini, P. Llanes, M.A. Pericàs and T. Noël, *Nat. Commun.*, **12**, 625 (2021); https://doi.org/10.1038/s41467-020-20882-x
116. P.L. Meena, A.K. Surela, K. Poswal, J.K. Saini and L.K. Chhachhia, *Biomass Convers. Biorefin.*, **14**, 3793 (2024); https://doi.org/10.1007/s13399-022-02605-y
117. P.B. Chouke, K.M. Dadure, A.K. Potbhare, G.S. Bhusari, A. Mondal, K. Chaudhary, V. Singh, M.F. Desimone, R.G. Chaudhary and D.T. Masram, *ACS Omega*, **7**, 20983 (2022); https://doi.org/10.1021/acsomega.2c01745
118. T. Li, S. Quan, X. Shi, L. Yang and C. Liu, *Catal. Lett.*, **150**, 640 (2020); https://doi.org/10.1007/s10562-019-02970-w
119. H. Chen, C. Yu, Z. Xue, P. Wang, Z. Wang, Q. Cong, L. Pei and C. Fan, *Toxicol. Environ. Chem.*, **102**, 356 (2020); https://doi.org/10.1080/02772248.2020.1798448
120. W. Zhang, S. Gao and D. Chen, *J. Rare Earths*, **37**, 726 (2019); https://doi.org/10.1016/j.jre.2018.12.007
121. G.K. Dinesh, S. Anandan and T. Sivasankar, *Environ. Sci. Pollut. Res. Int.*, **23**, 20100 (2016); https://doi.org/10.1007/s11356-015-5951-z
122. S. Zhu, L. Lu, Z. Zhao, T. Wang, X. Liu, H. Zhang, F. Dong and Y. Zhang, *J. Phys. Chem. C Nanomater. Interfaces*, **121**, 9394 (2017); https://doi.org/10.1021/acs.jpcc.7b01608
123. G. Viruthagiri and P. Kannan, *J. Mater. Res. Technol.*, **8**, 127 (2019); https://doi.org/10.1016/j.jmrt.2017.06.011
124. M. Prakash, H.P. Kavitha, S. Arulmurugan, J.P. Vennila, S. Abinaya, D. Lohita and R. Suresh, *J. Sol-Gel Sci. Technol.*, **110**, 807 (2024); https://doi.org/10.1007/s10971-024-06400-1
125. S.D. Khairnar, A.N. Kulkarni, S.G. Shinde, S.D. Marathe, Y.V. Marathe, S.D. Dhole and V.S. Shrivastava, *J. Photochem. Photobiol.*, **6**, 100030 (2021); https://doi.org/10.1016/j.jpap.2021.100030
126. I.M. Sharaf, M.S.I. Koubisy, F.H. Alkallas, A.B.G. Trabelsi and A.M. Aboraia, *Catalysts*, **15**, 519 (2025); https://doi.org/10.3390/catal15060519
127. R. Ji, C. Ma, W. Ma, Y. Liu, Z. Zhu and Y. Yan, *New J. Chem.*, **43**, 11876 (2019); https://doi.org/10.1039/C9NJ02521A
128. A.K. Berekute, K.P. Yu and Y.H. Chuang, *Sustain. Environ. Res.*, **32**, 17 (2022); https://doi.org/10.1186/s42834-022-00129-8
129. S. Iqbal, M. Iqbal, A. Sibtain, A. Iqbal, Z.H. Farooqi, S. Ahmad, K. Mustafa and S. Musaddiq, *Desalination Water Treat.*, **216**, 140 (2021); https://doi.org/10.5004/dwt.2021.26796
130. S. Sharma, S.K. Mehta, A.O. Ibhadon and S.K. Kansal, *J. Colloid Interface Sci.*, **533**, 227 (2019); https://doi.org/10.1016/j.jcis.2018.08.056
131. A.N. Shafawi, R.A. Mahmud, K. Ahmed Ali, L.K. Putri, N.I. Md Rosli and A.R. Mohamed, *J. Photochem. Photobiol. Chem.*, **389**, 112289 (2020); https://doi.org/10.1016/j.jphotochem.2019.112289
132. K.M. Chavan, V.A. Mane, N.D. Raskar, D.V. Dake, R.B. Sonpir and B.N. Dole, *ChemistrySelect*, **9**, e202403806 (2024); https://doi.org/10.1002/slct.202403806
133. M. Alahmadi, W.H. Alsaedi, W.S. Mohamed, H.M.A. Hassan, M. Ezzeldien and A.M. Abu-Dief, *J. Taibah Univ. Sci.*, **17**, 2161333 (2023); https://doi.org/10.1080/16583655.2022.2161333
134. T.A. Gadhi, S. Hernández, M. Castellino, P. Jagdale, T. Husak, A. Hernández-Gordillo, A. Tagliaferro and N. Russo, *Catal. Today*, **321-322**, 135 (2019); https://doi.org/10.1016/j.cattod.2017.12.038
135. J. Gao, S. Rao, X. Yu, L. Wang, J. Xu, J. Yang and Q. Liu, *J. Colloid Interface Sci.*, **628**, 166 (2022); https://doi.org/10.1016/j.jcis.2022.07.112
136. F. Shafiq, M.B. Tahir, A. Hussain, M. Sagir, J. Rehman, I. Kebaili, H. Alrobei and M. Alzaid, *Int. J. Hydrogen Energy*, **47**, 4594 (2022); https://doi.org/10.1016/j.ijhydene.2021.11.075
137. D.E. Mazouzi, F. Djani, A. Soukeur, W. Bouchal, A. Manseri, K. Derkaoui, A. Martínez-Arias, A. Ksouri, F. Şen and M.M. Kaci, *Surf. Interfaces*, **44**, 103581 (2024); https://doi.org/10.1016/j.surfin.2023.103581
138. Z. Khazaee, A.R. Mahjoub, A.H.C. Khavar, V. Srivastava and M. Sillanpää, *Environ. Sci. Pollut. Res. Int.*, **28**, 50747 (2021); https://doi.org/10.1007/s11356-021-14308-4
139. A. Meng, B. Zhu, Y. Zhong, S. Zhou, P. Han and Y. Su, *Energy Rev.*, **2**, 100052 (2023); https://doi.org/10.1016/j.enrev.2023.100052
140. D. Salazar-Marín, G. Oza, J.A.D. Real, A. Cervantes-Uribe, H. Pérez-Vidal, M.K. Kesarla, J.G.T. Torres and S. Godavarthi, *Appl. Surf. Sci. Adv.*, **19**, 100536 (2024); https://doi.org/10.1016/j.apsadv.2023.100536
141. Y. Wang, K. Du, R. Xu, D. Cui, Y. Shi, W. Hao and Y. Du, *Curr. Opin. Green Sustain. Chem.*, **41**, 100824 (2023); https://doi.org/10.1016/j.cogsc.2023.100824
142. Z. Han, Y. Song, Y. Jia, Y. Wang, J. Shi, X. Liu, L. Yu, Z. Li, Y. Cheng, H. Zhang and H.-Y. Jiang, *Adv. Mater. Interfaces*, **12**, 2500191 (2025); https://doi.org/10.1002/admi.202500191
143. V. Gurylev, *Mater. Today Sustain.*, **18**, 100131 (2022); https://doi.org/10.1016/j.mtsust.2022.100131
144. A. Gupta, B. Likozar, R. Jana, W.C. Chanu and M.K. Singh, *Int. J. Hydrogen Energy*, **47**, 33282 (2022); https://doi.org/10.1016/j.ijhydene.2022.07.210
145. P.E.A. Salomão, D.S. Gomes, E.J.C. Ferreira, L.L. Nascimento, F. Moura, A.O.T. Patrocínio and M.C. Pereira, *Sol. Energy Mater. Sol. Cells*, **194**, 276 (2019); https://doi.org/10.1016/j.solmat.2018.12.037

146. P.E.A. Salomão, L.R. de Souza Barbosa, T.S. Andrade, E.J. da Cruz Ferreira and M.C. Pereira, *Int. J. Hydrogen Energy*, **44**, 28603 (2019); https://doi.org/10.1016/j.ijhydene.2019.09.147
147. G. Yuan, N.B.S. Selabi, Y. Deng, Q. Jiang, Q. Li and J. Hu, *J. Environ. Chem. Eng.*, **14**, 121995 (2026); https://doi.org/10.1016/j.jece.2026.121995
148. F.H. Alkallas, A.B. Gouider Trabelsi, K.S. Almugren and M. Rabia, *Sci. Rep.*, **15**, 32434 (2025); https://doi.org/10.1038/s41598-025-16333-6
149. N.R. Khalid, Z. Israr, M.B. Tahir and T. Iqbal, *Int. J. Hydrogen Energy*, **45**, 8479 (2020); https://doi.org/10.1016/j.ijhydene.2020.01.031
150. T.T. Nguyen and K. Edalati, *Int. J. Hydrogen Energy*, **96**, 841 (2024); https://doi.org/10.1016/j.ijhydene.2024.11.353
151. F.-M. Fu, H.-D. Shen, W.-W. Xue, Y.-Z. Zhen, R. Soomro, X. Yang, D.-J. Wang, B. Xu and R. Chi, *J. Catal.*, **375**, 399 (2019); https://doi.org/10.1016/j.jcat.2019.06.033
152. H. Wang, Z. Zhao, Z. Asghar, X. Wang, J. Hou, M. Lin and J. Jia, *J. Alloys Compd.*, **1065**, 188055 (2026); https://doi.org/10.1016/j.jallcom.2026.188055
153. Y. Liu, J.-G. Guo, Y. Wang, Y.-J. Hao, R.-H. Liu and F.-T. Li, *Green Energy Environ.*, **6**, 244 (2021); https://doi.org/10.1016/j.gee.2020.04.014
154. W. He, Y. Wei, J. Xiong, Z. Tang, Y. Wang, X. Wang, J. Deng, X. Yu, X. Zhang and Z. Zhao, *Sep. Purif. Technol.*, **300**, 121850 (2022); https://doi.org/10.1016/j.seppur.2022.121850
155. S. She, B. Zhao, J. Wang, Z. Wei, X. Wu and Y. Li, *Sep. Purif. Technol.*, **309**, 123064 (2023); https://doi.org/10.1016/j.seppur.2022.123064
156. G. Xu, X. Guan, X. Wang, C. Zhang, X. Zhang, J. Liu, R. Li and C. Fan, *Mater. Lett.*, **349**, 134806 (2023); https://doi.org/10.1016/j.matlet.2023.134806
157. W. Dai, P. Wang, J. Long, Y. Xu, M. Zhang, L. Yang, J. Zou, X. Luo and S. Luo, *ACS Catal.*, **13**, 2513 (2023); https://doi.org/10.1021/acscatal.2c05724
158. H. Tang, X. Wang, C. Yao and Z. Zhang, *Separ. Purif. Tech.*, **338**, 126544 (2024); https://doi.org/10.1016/j.seppur.2024.126544
159. H. Han, S. Zhang, S. Song, W. Zhang, D. Liu, Z. Song, Q. Wang, C. Ma, S. Feng and X. Duan, *Appl. Surf. Sci.*, **662**, 160122 (2024); https://doi.org/10.1016/j.apsusc.2024.160122
160. A. Amari, H.S.S. Aljibori, Z. Algarni, N. Elboughdiri, M.A. Diab, K.-H. Baek and I. Mahariq, *J. Ind. Eng. Chem.*, **140**, 599 (2024); https://doi.org/10.1016/j.jiec.2024.08.002
161. N. Ojha and K.K. Pant, *ChemSusChem*, **18**, e202401260 (2025); https://doi.org/10.1002/cssc.202401260
162. W. Guo, Y. Zhang, J. Tian, Z. Liu, B. Liu and J. Li, *Nat. Commun.*, **17**, 983 (2025); https://doi.org/10.1038/s41467-025-67718-0
163. Y. Zhang, M. Hu, Y. Liu, C. Hu, Z. Wang, X. Bo and Y. Ma, *ACS Appl. Energy Mater.*, **9**, 5434 (2026); https://doi.org/10.1021/acsaem.6c00665
164. Q. Chen, J. Jiang, Y. Wu, J. Fang, N. Lu, G. Wang and J. Mao, *Chem. Eng. J.*, **504**, 158854 (2025); https://doi.org/10.1016/j.cej.2024.158854